

SPECIAL COLLECTION: FROM MAGMAS TO ORE DEPOSITS

Geochemistry of the Cretaceous Kaskanak Batholith and genesis of the Pebble porphyry Cu-Au-Mo deposit, Southwest Alaska

NANSEN H. OLSON^{1,*}, JOHN H. DILLES¹, ADAM J.R. KENT¹, AND JAMES R. LANG²

¹Geology, Oregon State University, 104 Wilkinson Hall, Corvallis, Oregon 97331, U.S.A.

²Hunter Dickinson, Inc., 1040 West Georgia Street, Vancouver, British Columbia V6E 4H1, Canada

ABSTRACT

The key magmatic processes that lead to the formation of large magmatic-hydrothermal porphyry copper mineral deposits remain uncertain, and a particular question is why a few of these deposits, such as the Pebble porphyry Cu-Au-Mo deposit, are strongly enriched in both gold and molybdenum. This study investigated the igneous rocks of the Pebble district and obtained major and trace element compositions, Sr and Nd isotopic compositions, and zircon age and trace element data to model the origin of the ore-forming magmas.

The Pebble porphyry Cu-Au-Mo deposit, one of the world's largest Cu-Au resources, formed during the final stages of regional Late Cretaceous arc magmatism (101–88 Ma) in the Southwest Alaska Range. Local pre-mineral intrusions (99–95 Ma) are dominated by alkaline compositions including monzodiorite stocks, shoshonite dikes, and monzonite porphyries, but also include lesser volumes of high-K calc-alkaline diorite and granodiorite sills. The occurrence of early alkaline magmas has been noted at other gold-rich porphyry systems, including Bingham and Kerr-Sulfurets-Mitchell. Mineralization at Pebble is associated with granodiorite to granite porphyry dikes related to the >165 km² high-K calc-alkaline Kaskanak granodiorite batholith (91–89 Ma). Over a period of 10 m.y., Late Cretaceous melts evolved from high temperatures (930–730 °C) and modestly hydrous and oxidized conditions to relatively low temperatures (760–680 °C) and very hydrous and oxidized conditions. Collectively, all Late Cretaceous igneous rocks at Pebble contain magnetite and little or no ilmenite, are metaluminous to weakly peraluminous, and have typical arc trace element enrichments and depletions. They have moderate Sr/Y ratios (20–55) and gently sloped REE profiles (La/Yb = 5–20) that are not adakitic, which supports a source area lacking garnet that is consistent with a thin crust in southwest Alaska.

Radiogenic isotopes for Late Cretaceous intrusions at Pebble have a restricted range of primitive Sr and Nd isotopic compositions ($^{87}\text{Sr}/^{86}\text{Sr}_\text{i} = 0.70329$ –0.70424; $\epsilon_{\text{Nd},\text{i}} = 4.9$ –6.1), which overlap with volcanic and plutonic basement rocks of the Jurassic Talkeetna Arc along the Alaska Peninsula. The Kaskanak batholith intrudes the Late Jurassic–Early Cretaceous Kahiltna flysch, and mixing models using Sr and Nd isotopes indicate that the Kaskanak batholith assimilated ≤10 wt% Kahiltna flysch in amounts that did not likely affect magma fertility. Xenocrystic zircon samples are abundant in Cretaceous pre-mineral intrusions and have U-Pb ages similar to detrital zircon samples in the Kahiltna flysch. These data support some assimilation of upper crustal Kahiltna flysch, but the dominance of Devonian–Mississippian xenocrystic zircon populations in some intrusions suggests derivation from unexposed older basement.

The extraordinary endowment of Cu and Au at Pebble is inferred to result from primitive calc-alkaline and alkaline arc magmas and the hydrous and strongly oxidized conditions that suppressed the formation and fractionation of Cu- and Au-enriched sulfide melts. Furthermore, differentiation to silicic compositions was a product of extensive crystal fractionation of parental melts accompanied by minor crustal assimilation. The trace element content of the intermediate composition intrusions indicates that both hornblende and titanite fractionation processes in the mid- to shallow-crust were both required to produce the more evolved granodiorite and granite porphyry compositions. Despite the apparent lack of Mo-enriched continental crust in the region, primitive hydrous melts were produced by protracted arc magmatism and were modified by minor crustal assimilation including early alkaline magmatism, periodic recharge of mafic hydrous basalts and hybrid andesites, and fractional crystallization, which was apparently sufficient to enrich Mo in late stage felsic melts.

Keywords: Pebble, Kaskanak, porphyry, Cu-Au-Mo, southwest Alaska, SW Alaska Range, Cretaceous

INTRODUCTION

The Pebble porphyry Cu-Au-Mo deposit in southwest Alaska (Fig. 1) is one of the world's largest Cu-Au-Mo-Ag mineral resources with 10.9 Bt ore containing 36.9 Mt copper, 2.53 Mt molybdenum, 3054 t gold, and 13 488 t silver, as well as abundant rhodium and minor palladium (Lang et al. 2013; Rebagliati and Lang 2015). Late Cretaceous magmatism of the Southwest (SW) Alaska Range belt (Fig. 1; Young et al. 1997; Hart et al. 2004; Goldfarb et al. 2013) spanned ~10 m.y. in the Lake Iliamna region and culminated with the intrusion of the Kaskanak batholith that consists largely of equigranular granodiorite and small volumes of granodiorite to granite porphyry dikes associated with ore formation.

Previous studies on the Pebble deposit have documented the geology and age of intrusions and ores (Bouley et al. 1995; Schrader 2001; Ricardo 2009; Gaunt et al. 2010; Lang et al. 2013; Olson 2015), interpretations from regional-scale aeromagnetic data (Anderson et al. 2014), the mineralogy, geochemistry, and

fluid-inclusion characteristics of hydrothermally altered rocks (Gregory et al. 2013; Harraden et al. 2013; Gregory 2017), and the radiogenic isotope characteristics of intrusions in the district (Ayuso et al. 2013; Goldfarb et al. 2013). In this contribution, we expand the petrological and geochemical data for magmatism in the Pebble district and include barren pre-ore calc-alkaline sills, pre-ore alkaline intrusions, the mineralized Kaskanak batholith, and post-ore Paleocene and Eocene hypabyssal dikes and intrusions. We examine the whole-rock major and trace elements, whole-rock Sr-Nd isotopic compositions, and rare earth element (REE) abundances of zircon and titanite from intrusions in the district to constrain the source of magmas and the role of assimilation and fractional crystallization (AFC) processes in generating the ore-forming magmas. Finally, we conclude with a discussion of the origin of the extraordinary metal endowment of Cu, Au, and Mo at Pebble and the likely key igneous processes that produced water, chloride, sulfur, and metal-rich melts from, which ore fluids were extracted.

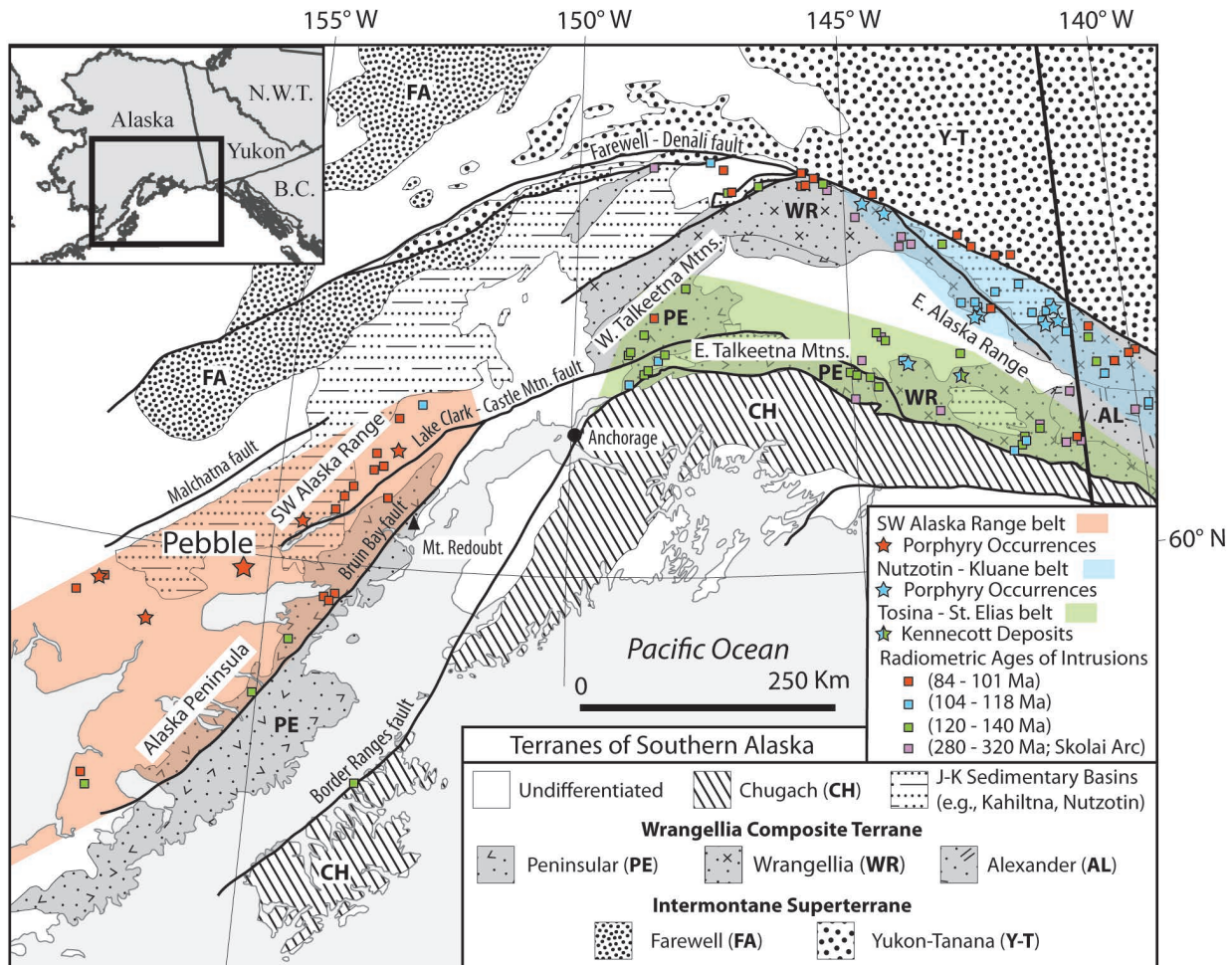


FIGURE 1. Simplified terrane map of southern Alaska (after Silberling et al. 1994). Selected Pennsylvanian and Cretaceous radiometric ages of intrusions in the Wrangellia composite terrane (WCT) are from Iriondo et al. (2003), Amato et al. (2007b), Bacon et al. (2012), and the USGS Mineral Resources Data System (MRDS) (<http://mrdata.usgs.gov/>). Porphyry occurrences are from Goldfarb et al. (2013) and the MRDS, and the Kennecott copper deposit (estimated age 155–110 Ma) is from MacKevett et al. (1997). Note that earliest Cretaceous magmatism in Tosina-St. Elias belt on the seaward margin of the WCT contains no known porphyry occurrences, but the younger Nutzotin-Kluane and SW Alaska Range belts of the landward margin of the WCT contain several porphyry deposits.

GEOCHEMICAL APPRAISALS OF ARC MAGMAS

Recent studies have developed many semi-quantitative geochemical techniques for assessing fertility of volcanic arc magmas on the basis of oxidation and hydration of the melt. In fertile volcanic arcs, parental magmas of large porphyry deposits are necessarily water-rich (>2.5 wt%, typically ≥ 4 wt%), oxidized (e.g., often $\geq \Delta \text{NNO} + 2$), rich in halogens (e.g., Cl/H₂O ≥ 0.5), anomalous in sulfur (e.g., Fe/S ≤ 100), and have experienced significant crystal-fractionation to increase chalcophile metal partitioning from the melt to the hydrothermal system (Burnham and Ohmoto 1980; Candela and Holland 1986; Dilles 1987; Cline and Bodnar 1991; Webster 1992; Candela 1992; Candela and Piccoli 2005; Richards 2011; Dilles et al. 2015). Redox sensitive proxies, such as Ce and Eu anomalies in zircon (Ballard et al. 2002; Trail et al. 2011; Dilles et al. 2015) or whole-rock V/Sc ratios (Loucks 2014) have also been utilized to infer oxidized conditions where Fe-Ti oxides are not present or preserved.

The petrographic context of these magmas is also critical for constraining and interpreting these geochemical proxies. For example, the presence of titanite in equilibrium with magnetite and quartz suggests highly oxidized melts (e.g., $\geq \Delta \text{NNO} + 2$, Dilles 1987; Wones 1989), and the presence of amphibole suggests minimum magmatic water contents of 3.5 wt% H₂O for granodiorite compositions at shallow crustal pressures (Naney 1983). The presence of amphibole and/or titanite can also greatly impact the high field strength element (HFSE) and rare earth element (REE) budget of differentiated melts (e.g., Kay and Mpodozis 2001; Richards and Kerrich 2007; Glazner et al. 2008; Bachmann and Bergantz 2008). Several workers (Seedorff et al. 2005; Richards and Kerrich 2007; Chiaradia et al. 2009; Richards 2011; Richards et al. 2012; Loucks 2014) have advocated the importance of high-water content in producing typical geochemical features of porphyry copper deposits and other hydrous arc magmas. Richards and Kerrich (2007) suggest high Sr/Y and La/Yb ratios in hydrous arc magmas are likely achieved by amphibole \pm titanite fractionation. Amphibole fractionation prevails at near-liquidus (high) temperatures because elevated water contents suppress plagioclase crystallization. These geochemical ratios are accentuated in thicker crust, but are also apparent, albeit less so, in thin crustal settings such as oceanic arcs (Richards and Kerrich 2007).

GEOLOGIC SETTING OF SOUTHWEST ALASKA

During the Jurassic to Early Cretaceous, the allochthonous Jurassic-Pennsylvanian Wrangellia composite terrane (WCT; Plafker et al. 1989) of oceanic arc affinity accreted to the North American plate and now makes up the bulk of southern Alaska (Fig. 1). In south-central and southeastern Alaska, the WCT consists of the Peninsular, Wrangellia, and Alexander terranes, whereas in the southwest Alaska only the Peninsular terrane is recognized. In southwestern Alaska, the suture zone between the Peninsular terrane and rocks of continental crustal affinity belonging to the Neoproterozoic-Paleozoic Farewell terrane, a part of the Intermontane belt superterrane, is obscured by younger sedimentary and igneous rocks and is therefore poorly delineated. Basement exposures of the Peninsular terrane consist of sedimentary formations (e.g., Triassic Kamishak and Jurassic Talkeetna Formations) and variably metamorphosed plutonic

and volcanic rocks of the Triassic Chilikadrotna Greenstones (flood basalts), other Triassic mafic and ultramafic intrusions (e.g., those from the Tlikakila Complex), and Jurassic intrusive and volcanic rocks of the Talkeetna Arc (Detterman and Reed 1980). Syn- to post-collisional volcaniclastic flysch deposits up to 5–7 km thick (Kalbas et al. 2007) overlie these basement rocks and were deposited in foreland basins in the Jurassic to Late Cretaceous (Csejtey et al. 1982; Jones et al. 1982, 1986; Coney and Jones 1985; Wallace et al. 1989; Kalbas et al. 2007; Hampton et al. 2010; Hults et al. 2013). In south-central and southwestern Alaska, these sedimentary strata are informally known as the Kahiltna flysch, noting that the southwestern-most portion of the basin is also known as the Koksetna River Sequence (e.g., Wallace et al. 1989). These sedimentary rocks comprise pelagic shales and turbidites of fine- to coarse-grained sandstones, siltstones, and minor pebble conglomerates composed of predominantly mafic to intermediate volcanic rock fragments with varying amounts of plagioclase, quartz, clinopyroxene, hornblende, epidote, and sedimentary rock fragments (Plafker et al. 1989; Wallace et al. 1989).

Concurrent with the development of flysch deposits but farther east in the Eastern Alaska Range, plutons of the Early Cretaceous Chisana arc (Barker 1987) intruded the Alexander and Wrangellia terranes (Fig. 1). The early part of this magmatic arc includes the Tosina-St. Elias belt (120–140 Ma), which occurs on the seaward margin of the WCT and contains no known porphyry occurrences. By approximately 120 Ma, Early Cretaceous magmatism had migrated northward to the landward margin of the WCT to form the Nutzotin-Kluane plutonic belt (104–118 Ma) that contains several minor porphyry deposits (Hart et al. 2004; Goldfarb et al. 2013). In the Late Cretaceous (101–88 Ma), intermediate to felsic intrusions of the SW Alaska Range plutonic belt were emplaced in the Western Talkeetna Mountains and Alaska Peninsula (Reed and Lanphere 1972; Detterman and Reed 1980; Young et al. 1997; Iriondo et al. 2003; Hart et al. 2004; Amato et al. 2007b; Goldfarb et al. 2013). The SW Alaska Range belt contains few known porphyry copper occurrences, but does include the giant Pebble porphyry deposit.

The SW Alaska Range belt consists predominantly of plutonic rocks and hypabyssal dikes (Reed and Lanphere 1972; Detterman and Reed 1980; Amato et al. 2007b) that intrude the Kahiltna flysch and the underlying Kamishak and Talkeetna formations of the Peninsular terrane (Detterman et al. 1996). Paleocene and Eocene volcanic rocks and Quaternary glacial sedimentary rocks are widespread in the SW Alaska Range and unconformably overlie and obscure Mesozoic rocks in the region.

GEOLOGY OF THE PEBBLE DISTRICT

In the Pebble district (Fig. 2), Late Cretaceous plutonic rocks span a 10 m.y. period that culminated with emplacement of porphyry dikes and stocks that are genetically linked to the formation of the Pebble porphyry Cu-Au-Mo deposit [see Olson (2015) for a complete chronological summary]. Exposures and drill intercepts indicate a >300 km² extent of Late Cretaceous plutonic rocks at Pebble, and some workers have suggested aeromagnetic data indicate an even larger extent (~900 km²) beneath volcanic and sedimentary cover (Anderson et al. 2014), thereby making it one of a few large Cretaceous plutonic complexes delineated

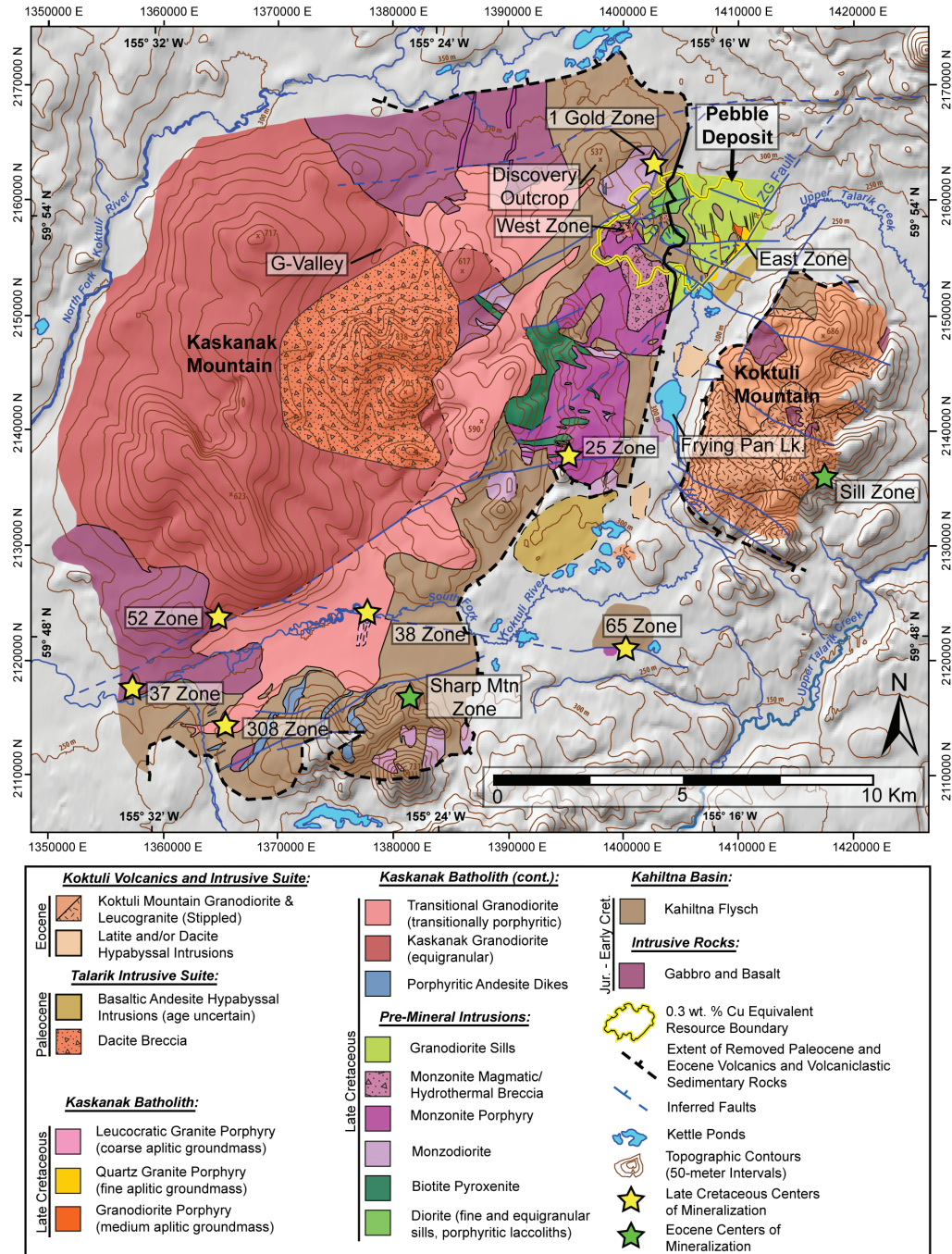


FIGURE 2. Late Cretaceous bedrock geology map of the Pebble district (modified after Lang et al. 2013). Paleocene and Eocene hypabyssal intrusions and granitic rocks are shown where they crosscut the Late Cretaceous basement, but Paleocene–Eocene volcanic and volcaniclastic cover rocks have been removed to illustrate the basement lithology where it has been intersected by drilling.

in the SW Alaska Range belt (Wilson et al. 2015). In the Pebble district, these intrusions are hosted by Early Cretaceous deposits of the Kahiltna flysch based on inherited zircons and crosscutting relationships (Lang et al. 2013). The oldest exposures of igneous rocks in the district include greenschist facies metabasalt and metagabbro roof pendants in the Kaskanak batholith, which likely represent Triassic–Jurassic basement rocks.

Pre-mineralization intrusions (ca. 99–95 Ma) are precursory to the emplacement of the Kaskanak batholith and are subdivided into two diverse magmatic suites: (1) calc-alkaline sills, and (2) alkalic stocks and porphyry dikes (Bouley et al. 1995; Schrader 2001; Gaunt et al. 2010; Hart et al. 2010; Lang et al. 2013). Biotite pyroxenite cumulate rocks (~96 Ma) occur with alkalic intrusive rocks in the 25 Zone primarily west of the ZG

fault trace (Fig. 2) and may represent the eroded roots of the alkalic magmatic system. There are no known intrusions with ages between 95 and 91 Ma in the district.

The Kaskanak batholith (91–89 Ma) is composed of calc-alkaline granodiorite, lesser granite and subordinate andesite intrusions genetically linked to multiple centers of porphyry copper and skarn mineralization. It includes at least three generations of weakly to strongly mineralized granodiorite to granite porphyry dikes and plugs (Fig. 2). The outlined resource boundary of the Pebble deposit includes two main mineralization centers known as the West Zone and East Zone (Fig. 3).

Late Cretaceous intrusions were exhumed to the surface in the latest Cretaceous, crosscut by a series of latest Late Cretaceous to Paleocene hypabyssal intrusions (ca. 67–58 Ma), and overlain by Paleocene (≤ 61 Ma; Olson 2015) volcaniclastic and tuffaceous strata. These previously unnamed hypabyssal intrusions and volcaniclastic sedimentary rocks are herein referred to as the Talarik Intrusive Suite and the Talarik Formation. These rocks may be correlative with the Copper Lake Formation (Detterman and Reed 1980; Detterman et al. 1996) and similar volcanic and volcaniclastic rocks described in the Dillingham Quadrangle (Iriondo et al. 2003; Wilson et al. 2003). Eocene hypabyssal intrusions and associated volcanic rocks (47–41 Ma) are exposed primarily on the east side of the district around Koktuli Mountain and are henceforth referred to as the Koktuli Intrusive Suite and the Koktuli Volcanics. These Eocene igneous rocks are likely part of the Eocene to earliest Miocene Meshik Arc (Wilson 1985;

Wilson et al. 2015). Some centers of epithermal mineralization in the district (Fig. 2) are associated with Eocene latite dikes (Fig. 3b; Bouley et al. 1995).

The structural history of the Pebble district is complex. Geologic observations indicate that extension, tilting, and normal faulting occurred during deposition of the Talarik Formation and the Koktuli Volcanics (Olson 2015). The northeast-striking ZG Fault bounds the western side of the East Graben, has the largest observed offsets, and is one of the oldest normal faults recognized in the district (Figs. 2 and 3; Olson 2015). Eocene and younger hypabyssal intrusions and orthogonal normal faulting dissect the ZG fault (Olson 2015). Collectively, normal faulting in the district has produced ~20° eastward rotation (Fig. 3).

ANALYTICAL METHODS

Whole-rock analyses

In total, 108 whole-rock major and trace element analyses were performed at Washington State University's (WSU) GeoAnalytical Lab using both XRF (Johnson et al. 1999) and ICP-MS methods (Knaack et al. 1994). These samples were collected from drill core and, to the extent possible, were selected to minimize the effects of hydrothermal alteration. For many alteration-sensitive plots (e.g., A/NCK, Sr, etc.), additional samples were culled using Ishikawa alteration index (AI) values ≥ 60 (Ishikawa et al. 1976; Large et al. 2001; AI = molar 100 $[K_2O+MgO]/[K_2O+MgO+Na_2O+CaO]$) and LOI values ≥ 3.5 wt%. See Appendix¹ A for the

¹Deposit item AM-17-86053, Tables 3 and 4 and Supplemental Appendices. Deposit items are free to all readers and found on the MSA web site, via the specific issue's Table of Contents (go to http://www.minsocam.org/MSA/AmMin/TOC/2017/Aug2017_data/Aug2017_data.html).

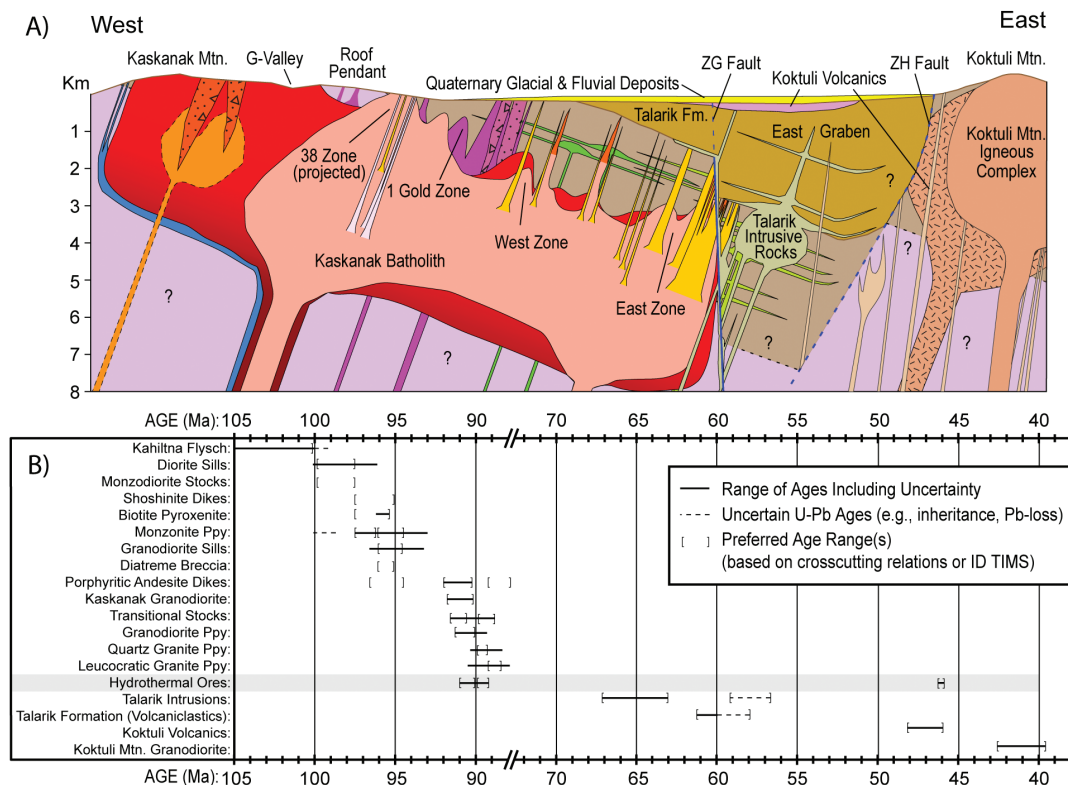


FIGURE 3. (a) Schematic east-west cross section and geologic reconstruction of the Pebble district interpreted from available drill core data (Olson 2015). Lithologies as in Figure 2 or as labeled. Intrusion geometries, crosscutting relations, and fault relationships east of the ZG fault are highly interpretative and based on scarce drill data. (b) Summary of inferred intrusion ages based on radiometric ages and crosscutting relations.

TABLE 1. Petrography of Pebble District igneous rocks

Lithology	Texture(s)	Primary mineralogy (vol%)
Gabbro	Fine- to medium-grained and subophitic	60–70% plag (0.25–1 mm, rarely up to 5 mm), 15–20% cpx (0.5–2.5 mm), 8% mag (0.25–1.5 mm), 2% ilm (0.2–0.5 mm), acc. apa
Basalt	Hypocrystalline, porphyritic, interstitial	60–70% plag (0.2–5 mm), 10–15% glass, 5–10% mag (0.5 mm), 10% cpx (0.2–0.5 mm),
Diorite Sills	Granular to porphyritic	60% plag (0.5–1.5 mm), 15–20% gm (0.05–0.1 mm; feldspar > qtz), 10–15% primary amph or cpx & bt (1.5–3 mm), 2–1–3% mag (0.05–0.15 mm), <2% apa (0.1–1 mm), acc. zir
Monzodiorite Stocks	Seriate, poikilitic K-felds	50–55% plag (0.2–2 mm), 15–20% K-felds (2–4 mm), 15% cpx (0.1–2 mm), 10% primary bt (0.1–4 mm), and 2–5% mag (0.1–0.3 mm)
Biotite Pyroxenite	Cumulate cpx, intercumulate bt and mag	70% cpx (0.25–1.5 mm, sometimes as large as 7 mm), 15% bt (0.5–1.5 mm), 15% mag (0.1–0.5 mm), acc. plagioclase (0.1–0.3 mm) and apa
Monzonite Porphyry	Porphyritic, albitic coronas on plag (emphasized by preferentially illite-altered cores)	50–70% cryptocrystalline gm, 25–40% plag (0.5–6 mm), 5–15% K-felds (commonly 1–2 mm, up to 10 mm), 5–10% cpx (0.5–2 mm), 5–10% primary bt (0.5–1 mm), rare accessory zircon
Monzonite Porphyry w/ megacrystic K-feldspar	Porphyritic, poikilitic K-feldspar, albitic coronas on plag (emphasized by preferentially illite-altered cores)	30–50% cryptocrystalline to microcrystalline gm (up to 0.3 mm containing plag > K-felds > bt), 20% plag (2–3 mm), 20–30% K-felds (commonly 1–2 cm, up to 7 cm), 5–10% total mafics [bt+cpx] (0.5–4 mm), 1–2% mag (0.05–0.2 mm), <0.5% apa (0.1–0.5 mm), rare acc. tit and zir
Shoshonite Dikes	Glomeroporphyritic	40–50% plag (0.5–1.5 mm), 15–20% gm (0.1–0.2 mm plag + K-felds), 10–15% cpx (1–2 mm), 5–8% mag (0.5–0.1 mm), 5–10% bt (0.5–3 mm), acc. apa (<0.3 mm)
Granodiorite Sills	Granular to porphyritic, some sieve-textured plag with albitic coronas	40–50% plag (0.5–2 mm), 30–40% aplitic gm (0.05 mm), 5–10% amph/bt (1–3 mm), 2% mag (0.1–0.3 mm), 0–1% qtz phenocrysts (0.5–1 mm), ≤1% apa (<0.1 mm), acc. zir
Porphyritic Andesite Dikes	Porphyritic, cryptocrystalline gm in 1 Gold Zone, micro-crystalline gm near 308 Zone, sieve-textured plag with albitic coronas	1 Gold Zone: 50–60% plag (0.1–0.5 mm), 20% cryptocrystalline gm, 8–10% amph (0.1–1 mm), 1–2% mag (0.02–0.1 mm), acc. apa; 308 Zone: 45% plag (0.5–3 mm), 35–45% fine gm (plag > K-spar > amph) (0.01–0.05 mm), 10–12% amph (1–7 mm), 2–3% mag (0.02–0.1 mm), acc. apa, zir, microcline (0.5–1 mm)

Notes: Units are listed by age from oldest to youngest. Abbreviations: acc. = accessory, act = actinolite, amph = amphibole, apa = apatite, bt = biotite, calc = calcite, chl = chlorite, cpx = clinopyroxene, epi = epidote, gm = groundmass, hem = hematite, HT = hydrothermal, ilm = ilmenite, K-felds = K-feldspar, mag = magnetite, musc = muscovite, plag = plagioclase, qtz = quartz, smect = smectite, tit = titanite, zir = zircon.

(Table extends to next page)

complete whole-rock major and trace element compositions and sample locations. Strontium and neodymium isotopic compositions were determined for 12 samples at the University of Cape Town, South Africa, using methods described by Miková and Denkova (2007). Appendix 1 A and Table 2 provide additional analytical details.

In situ zircon and titanite analyses

Ten zircon separates were analyzed by the sensitive high-resolution ion-microprobe in reverse geometry (SHRIMP-RG) at the Stanford USGS Micro Analysis Center (SUMAC) to obtain U/Pb age and trace element compositions (Appendix 1 B). Spot sizes for individual analyses were approximately 25 μm diameter and 1–2 μm deep allowing for sampling of high-uranium zones while avoiding cracks, apatite inclusions, and melt inclusions (Mazdab and Wooden 2006). ^{207}Pb -corrected $^{206}\text{Pb}/^{238}\text{U}$ spot ages were standardized using the R33 age standard with an assigned age of 420 Ma (Mattinson 2005). Trace element data were standardized to the MAD and MADDER zircon reference standards of similar composition developed by the SUMAC Laboratory (Mazdab and Wooden 2006; Wooden and Barth 2010).

An additional 22 zircon separates and 3 samples of titanite from igneous rocks were analyzed by laser ablation inductively coupled plasma mass spectrometry (LA-ICP-MS) in the W.M. Keck Collaboratory at Oregon State University to obtain U/Pb ages and trace element compositions (Appendix 1 C). A Photon Machines Analyte G2 193 nm laser and a Thermo-XseriesII Quadrupole mass spectrometer equipped with an ion counter were used for ICP-MS analyses. Ablation spot diameters ranged between 30 and 40 μm in zircon and were 50 μm in titanite. ^{207}Pb -corrected $^{206}\text{Pb}/^{238}\text{U}$ spot ages were standardized using the R33 age standard with an assigned age of 420 Ma (Mattinson 2005). Reproducibility indicated by the relative percent of the standard error of the mean (SE%) of the R33 standard for N = 6 to N = 9 analyses on 17 analytical sessions ranges from $\pm 0.8\%$ to $\pm 2.0\%$. Analyses of a secondary age standard, TEMORA 1 (416.8 ± 1.1 Ma; Black et al. 2003), treated as unknowns and analyzed over the 17 analytical sessions (N = 51) produce a mean age of 421.6 Ma with a SE of 2.8 m.y., which overlaps the reported age at the 95% confidence level. Zircon trace element data were processed using in-house LaserTram software (Loewen and Kent 2012). Zircon data were rigorously screened to remove analyses that encountered apatite inclusions by monitoring for elevated phosphorous and light

rare earth element contents. Zircon trace element data were standardized to NIST-612 glass for Nb, La, Pr, Ho, and Tm, and to the MADDER zircon reference standard (see above) for all other trace elements. Titanite trace element data were standardized to the USGS GSE-1G geochemical reference standard and are reported in Appendix 1 D.

Calculated Eu and Ce anomalies

The magnitude of the redox-sensitive Eu and Ce anomalies can be quantified by the expressions: $\text{Eu/Eu}^* = \text{Eu}_{\text{CN}}/[\text{Sm}_{\text{CN}}^{(1/2)} \text{Gd}_{\text{CN}}^{(1/2)}]$ and $\text{Ce/Ce}^* = \text{Ce}_{\text{CN}}/[\text{La}_{\text{CN}}^{(2/3)} \text{Nd}_{\text{CN}}^{(1/3)}]$ where CN refers to chondrite-normalized values (McDonough and Sun 1995). However, the Ce anomaly is difficult to measure accurately due to large analytical uncertainties and limits of determination for low-abundance La or Pr in zircon by SIMS or LA-ICP-MS methods. Instead of using the Ce/Ce* calculation, we have used the Ce/Nd ratio as a proxy for the Ce anomaly following initial proposals by Olson (2015) and Lu et al. (2016).

Calculated zircon and titanite temperatures

Ti-in-zircon and Zr-in-titanite temperatures can be estimated for the melt if the activities of TiO_2 and SiO_2 , and the pressure of crystallization can be estimated where $T^{\text{Zr}}(\text{°C}) = -(4800 \pm 86)/[\log(\text{Ti ppm}) - (5.711 \pm 0.072) + \log(\alpha_{\text{SiO}_2}/\alpha_{\text{TiO}_2})] - 273.15$ and $T^{\text{Ti}}(\text{°C}) = [7708 + 960 \cdot P(\text{GPa})]/[10.52 - \log(\alpha_{\text{TiO}_2}/\alpha_{\text{SiO}_2}) - \log(\text{Zr ppm})] - 273.15$ (Ferry and Watson 2007; Hayden et al. 2008). Estimates of 0.5–0.7 for α_{TiO_2} are generally appropriate for most volcanic arc magmas that are buffered by Ti-bearing phases (e.g., ilmenite or titanite) and an estimate of $\alpha_{\text{SiO}_2} = 1.0$ is appropriate for quartz-saturated igneous rocks (Watson et al. 2006; Claiborne et al. 2010; Walker et al. 2013). Underestimations of the α_{TiO_2} may cause a maximum decrease in Ti-in-zircon temperatures of 20 °C (Watson et al. 2006; Claiborne et al. 2010), and a maximum increase in Zr-in-titanite temperatures of 20 °C (Hayden et al. 2008). Errors of 0.1 GPa in the pressure estimates would cause a systematic 10–15 °C shift in Zr-in-titanite temperatures at 700–800 °C. The largest single contributor of uncertainty is caused by zircon and titanite sector zoning that may skew temperature calculations by ± 15 –20 °C in zircon (Dilles et al. 2015) and up to ± 50 –70 °C in titanite between the temperature range of 700 and 800 °C (Hayden et al. 2008).

TABLE 1.—EXTENDED

Lithology	Texture(s)	Primary mineralogy (vol%)
Kaskanak Granodiorite	Hypidiomorphic-granular, poikilitic K-felds, consertal qtz, early bt occurs dominantly as inclusions in amph with reaction rims, ilm only occurs as inclusions in bt	50–60% plag (0.5–3 mm), 15–20% K-felds (1–20+ mm), 10–12% amph (1–5 mm), 5–10% qtz (0.25–1.5 mm), 2–3% mag (0.5–1 mm), up to 1% primary bt (0.2–2 mm), and accessory ilm (<0.2 mm), tit (0.3–1 mm), zir (50–120 mm), and apa (50–300 mm). Note: microprobe analyses on plag yield andesine, and analyses of amph yield low-Al magnesio-hornblende.
Transitional Granodiorite	Porphyritic with consertal and graphic qtz + K-felds interstitially (0.3–1 mm), lacks significant gm (\leq 15%), hiatal amph phenos	50–65% plag (0.5–5 mm), 8–10% amph (commonly 1–3 mm, up to 10 mm), variably 5–15% aplitic gm (>0.2 mm), 10% K-felds (0.3–20 mm), 5–10% interstitial quartz (0.25–1 mm), tr–3% qtz phenocrysts (0.5–1 mm), 1–2% mag (0.5–1 mm), and acc. tit (0.3–1 mm), apa, and zir
Granodiorite Porphyry	Porphyritic with medium aplitic gm (0.1–0.3) mm	55–60% plag (0.3–3 mm), 20% medium aplitic gm (0.1–0.3 mm), 8–10% amph (0.5–4 mm), 1–2% mag (0.2–0.5 mm), and acc. rare qtz phenocrysts (0.25–0.5 mm), apa, zir, tit
Quartz Granite Porphyry	Porphyritic with variable amounts of fine (aphanitic) aplitic gm (0.02–0.05 mm), except in 38 & 308 zones: fine to medium aplitic gm (0.05–0.15 mm)	40–60% (0.5–4 mm) plag, 25–50% fine aplitic gm (0.02–0.05 mm), 5–8% amph (commonly 0.5–2 mm, up to 5 mm), 0–2% (0.5–1.5 mm) qtz phenocrysts, and 0–5% K-spar phenocrysts (2–3 mm), acc. mag (0.2–0.5 mm), zir, apa, tit (0.3–1.2 mm)
Leucocratic Granite Porphyry	Porphyritic with coarse aplitic gm (0.1–0.3 mm) to cryptocrystalline gm (<0.01 mm)	45–50% coarse aplitic gm (0.1–0.3 mm), 35–40% plag (2–5 mm), 2–3% qtz (1–3 mm), 2–3% K-felds (3–5 mm), 2–3% mag (0.25–0.5 mm), 2–3% amph pseudomorphs (0.5–1 mm), acc. apa and zir
Paleocene Dacite Dikes	Porphyritic, weak flow banding, microcrystalline to cryptocrystalline gm (<0.01 mm)	95% gm (<0.01 mm, feldspar >> HT bt), 5% plag (0.1–2 mm), acc. mag, apa, zir
Paleocene Andesite Dikes	Porphyritic, sieve-textured plag with albitic coronas	65–70% gm (0.01–0.05 mm), 15% plag (0.1–1 mm), 15% acicular amph (0.2–5 mm), mag (3–4%) (0.02–0.03 mm), acc. apa, zir
Paleocene- Eocene Basaltic Andesite Dikes	Porphyritic, hypocrystalline, glass is devitrified	60% devitrified glass, 20–25%, plag (0.05–0.5 mm), 8–10% acicular amph (0.1–2.5 mm), 1–3% mag (0.02–0.5 mm), acc. apa
Eocene Koktuli Mountain Grandiorite & Alaskite	Equigranular alaskite, Hypidiomorphic-granular to seriate or porphyritic granodiorite, alaskite xenoliths and crystal cargo abundant in granodiorite	Coarse phase (alaskite): 70–75% anhedral K-felds (1–5 mm), 10% subhedral plag (1–3 mm), 10% consertal/graphic qtz (0.1–1 mm), 3–4% mag (0.1–0.3 mm), 2–3% acicular amph (0.5–1 mm), acc. apa, zir; Medium and fine phases (granodiorite): 70% plag (0.2–3 mm), 10% K-felds (0.2–1 mm), 8–10% acicular amph (0.2–2 mm), 5% interstitial qtz (0.2–0.5 mm), 1–2% mag (0.2–0.5 mm), acc. apa, zir

RESULTS

Petrography and mineralogy

Major and accessory mineral phases and textures of igneous rocks in the Pebble district (Olson 2015) are summarized in Table 1 and provide constraints for mineral-melt trace-element partitioning and melt evolution for Pebble district intrusions. Most pre-mineral Late Cretaceous intrusions (99–95 Ma) are medium-grained and hypidiomorphic-granular, but volumetrically, most alkalic rocks include monzonite porphyry with phenocrysts up to 6 mm and a groundmass with a grain size <0.3 mm (Table 1). The mineralogy of the bulk of these pre-mineral intrusions is dominated by plagioclase, biotite, and augite, with accessory magnetite and apatite. The latest of these intrusions (e.g., late monzonite porphyries and granodiorite sills) have nearly subequal quantities of biotite and amphibole but lack augite, and this change reflects an increase of magmatic water content with time. Rare diamond-shaped mineral sites containing hydrothermal magnetite are found in some of the most differentiated monzonite porphyries and are inferred to be pseudomorphs of igneous titanite. Ilmenite is not observed in any of the pre-mineral Cretaceous intrusive rocks, but small amounts may have originally been present and later hydrothermally altered (Olson 2015).

The bulk of the Kaskanak batholith is composed of granodiorite that ranges from medium-grained hypidiomorphic granular to strongly porphyritic in texture. These rocks contain abundant plagioclase and amphibole, minor K-feldspar and quartz with accessory magnetite (2–3 vol%), biotite (<1 vol%), and titanite

(0.5–2.0 vol%), and is interpreted to be more oxidized and hydrous than the pre-mineral intrusions based on the abundance of titanite and amphibole. Mineralized porphyry dikes are characteristically crystal-rich and contain \geq 75 vol% phenocrysts in early granodiorite porphyry and \geq 50 vol% in late quartz granite porphyry. Quartz and K-feldspar phenocrysts are absent from early granodiorite porphyry but are present up to 2 vol% of each in late granite porphyry. Porphyritic phases of the Kaskanak batholith have a fine-grained groundmass dominated by quartz and K-feldspar that ranges from 0.3–1 mm graphic texture in “transitional” granodiorite and 0.02–0.3 mm aplitic texture in porphyry intrusions.

Whole-rock geochemistry

Jurassic(?) mafic roof pendants. Basalt and gabbro bodies occur as roof pendants of the Kaskanak batholith and Koktuli Mountain pluton (Fig. 2). Locally, the basalt crosscuts and includes inclusions of the gabbro. Their major and trace element compositions share similarities with mafic volcanic and plutonic rocks (<55 wt% SiO₂) of the Jurassic Talkeetna Arc in the Talkeetna Mountains (Clift et al. 2005; Greene et al. 2006) and the gabbronorites of the Tonsina mafic-ultramafic root of the Talkeetna arc in the Peninsular terrane (DeBari and Sleep 1991). Collectively, they are all tholeiitic, have moderate Mg numbers = 30–45), and are ilmenite-bearing. The gabbro and basalt in the Pebble district are relatively enriched in Ti, Ni, Cr, and V (Figs. 5 and 7) compared to most other Talkeetna Arc volcanic and plutonic rocks, and thus are more primitive. They are also relatively enriched in HFSEs such as Nb, Ta, Zr, and

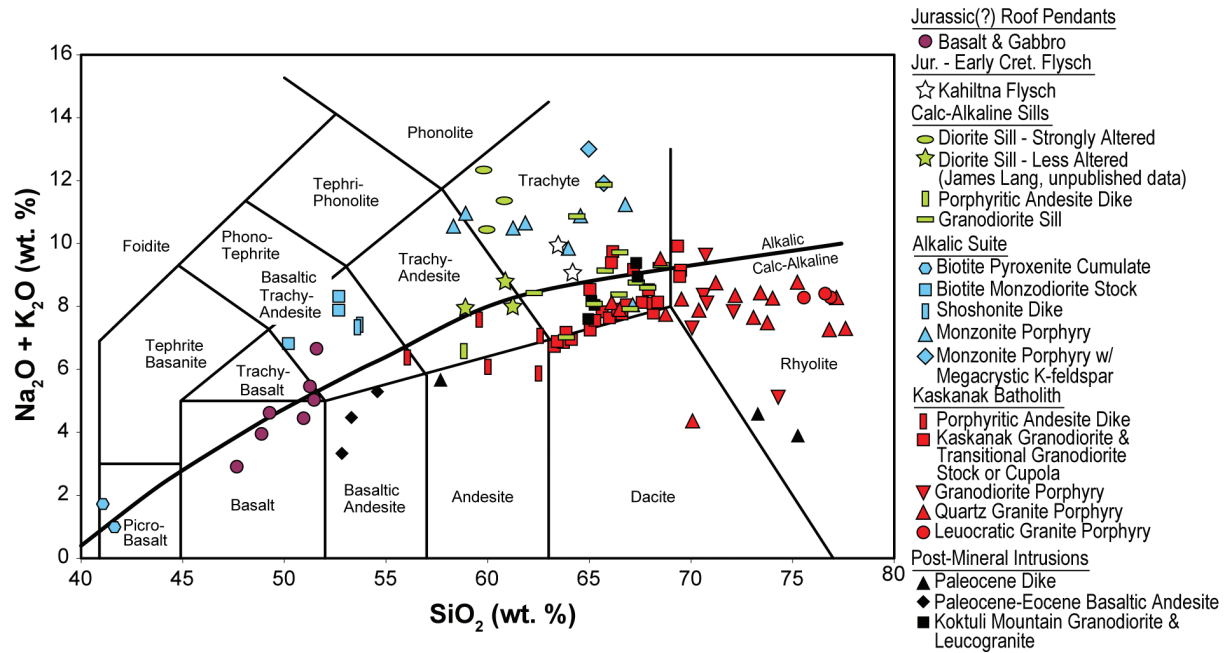


FIGURE 4. Total alkalis vs. silica for igneous and sedimentary rocks in the Pebble district (after Le Maitre et al. 1989; alkaline-subalkaline division of Irvine and Baragar 1971). Weakly altered diorite sill samples are from James Lang (written communication, 2012).

Hf (Appendix¹ A). Therefore, Pebble gabbro and basalt may be similar in composition and age to the Talkeetna Arc, but are most similar to the more primitive Tisina segment. Alternatively, they could be correlative with the Triassic Chilikadrotna Greenstones for, which comparative geochemical data are lacking (Detterman and Reed 1980; Wallace et al. 1989; Amato et al. 2007c). Similar enrichments in Ti, Ni, Cr, V, and HFSEs are observed in the mafic rocks of the Tlikakila Complex near Lake Clark, but these rocks all have higher Mg numbers ranging between 50 and 75 for similar compositions. They have been interpreted as primarily Late Triassic in age based on Norian fossils in sedimentary units (Wallace et al. 1989; Amato et al. 2007a), but the lower bounding age of plutonic rocks is inferred based on the sedimentary units, and thus it cannot be ruled out that some igneous components overlap with the Talkeetna Arc. Other lines of evidence such as Sr-Nd isotopes and detrital zircons (discussed later) suggest these rocks may not be directly correlative with the gabbro and basalt found in the Pebble district. Nevertheless, the elevated Ni (ca. 55–150 ppm) and Cr concentrations (ca. 115–465 ppm) in the Pebble basalt and gabbro distinguish them from the most primitive Late Cretaceous and younger intrusions in the district, which are basaltic andesites (Fig. 4). The Kahiltna flysch at Pebble also contains elevated Ni (ca. 27–34 ppm) and Cr (ca. 79–96 ppm) that likely reflects the composition of primitive regional mafic and ultramafic rocks as a detrital source.

Late Cretaceous igneous rocks. Late Cretaceous intrusions include three distinctive geochemical suites: high-K calc-alkaline sills, alkali stocks and dikes, and the late high-K calc-alkaline Kaskanak batholith. The geochemical differences distinguishing the three suites are described further below. All intrusions are magnetite-bearing, oxidized, and range in composition from metaluminous to weakly peraluminous with aluminum saturation

indices ($A/CNK \leq 1.1$) (Fig. 5). Trace elements are characterized by Nb, Ta, and Ti depletions typical of volcanic arcs (e.g., Ryerson and Watson 1987), and enrichments of large ion lithophile elements (LILE) and fluid-mobile elements (Sr, K, Cs, Rb, Ba, U, Th, Pb) compared to MORB (Fig. 6). The Sr/Y and La/Yb ratios of these intrusions are relatively low compared to porphyry deposit intrusions hosted by continental crust, but fall within typical ranges observed for porphyry deposit intrusions hosted by oceanic arc terranes (Fig. 7; Richards and Kerrich 2007). The V/Sc ratios of Late Cretaceous intrusions range from 10 to 160 and, except for the mafic end-members of the alkaline suite (<55 wt% SiO₂), are similar to or greater than the V/Sc ratios (10–20) typical of porphyry deposit magmas (Fig. 7; Loucks 2014). The V/Sc ratio increases gradually with increasing silica, which has been proposed by Loucks (2014) to reflect strongly oxidized magmatic conditions where significant vanadium occurs in oxidized V⁴⁺ and V⁵⁺ valences and behaves incompatibly in the melt. Most of the elevated V compositions are likely magmatic features, but a few samples have exceptionally elevated V concentrations up to 1600 ppm, likely as a result of hydrothermal enrichment (circled in Fig. 7). Hydrothermal enrichment of V in porphyry deposits has been proposed to preferentially occur in highly oxidized systems and where there has been considerable telescoping of the epithermal and porphyry hydrothermal footprints (Richards 1995; Loucks 2014).

The calc-alkaline diorite and granodiorite sills are the oldest and youngest pre-mineral intrusions in the district, respectively, and are temporally associated with alkalic intrusions (Lang et al. 2013; Olson 2015). The diorite and granodiorite sills have many similar trace element contents suggesting common origin that includes elevated Ti, Y, Yb, and P compared to other local Cretaceous and Tertiary rocks (Figs. 5 and 6). The diorite sills have

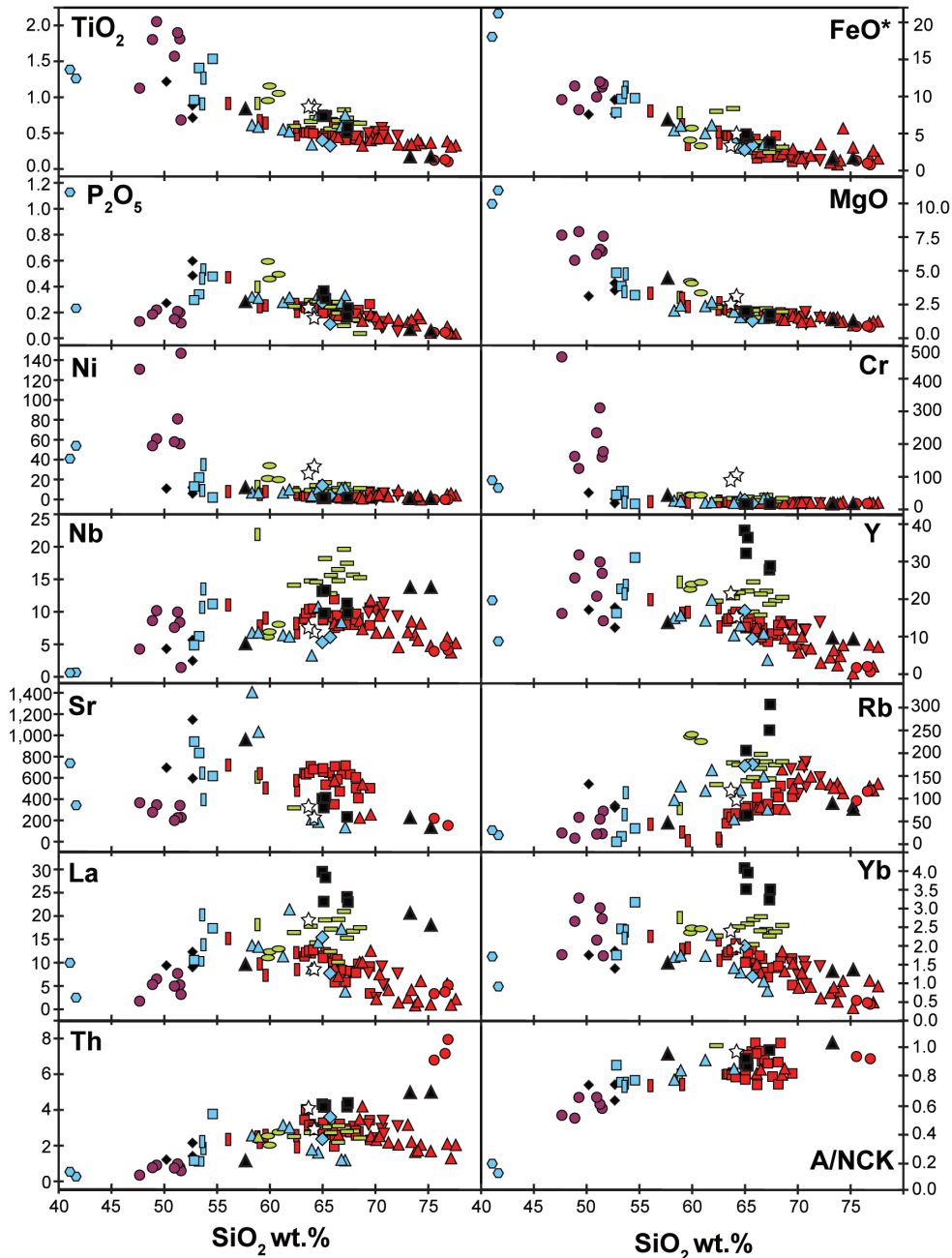


FIGURE 5. Selected major oxide (wt%) and trace element (ppm) variation as a function of SiO_2 (wt%). Samples with an Ishikawa Alteration Index > 60 (Large et al. 2001) were not included in plots of Sr and the A/NCK index. Symbols as in Figure 4.

much higher V, Sc, and Ni contents, a larger negative Eu anomaly, lower HFSE (Nb, Ta, Zr, Hf), and lower LREE (La, Ce) compared to the granodiorite sills (Figs. 5, 6, and 7). A single porphyritic andesite intrusion immediately west of the Pebble deposit closely shares trace element characteristics with the granodiorite sills and may be genetically related, but it differs from other rare occurrences of porphyritic andesite dikes sampled on the flanks of the Kaskanak batholith. Collectively, the geochemical differences among the pre-mineral calc-alkaline intrusive rocks may result

from both greater differentiation and minor assimilation of the Kahiltna flysch or mafic basement rocks.

The lithologically diverse alkalic suite includes monzodiorite and monzonite ranging from 50 to 67 wt% SiO_2 , and pyroxenite with 42 wt% SiO_2 . The HFSE and REE concentrations of the alkalic suite are mostly lower than the calc-alkaline sills and similar to the Kaskanak granodiorite (Figs. 6 and 8). Early monzodiorite stocks are spatially associated with biotite pyroxenite bodies interpreted as cogenetic cumulates. The biotite pyroxenite

cumulates have similar middle rare earth element (MREE) slopes and abundances to other alkalic intrusions, but they are relatively depleted in both light and heavy rare earth elements consistent with accumulation of MREE-enriched clinopyroxene. The biotite pyroxenite cumulates have concentrations of Ti, Ni, and Cr similar to other alkalic rocks, which are much lower than the concentrations observed in the basalt and gabbro roof pendants. Rare shoshonite dikes also occur and have similar compositions to the monzodiorite stocks (Fig. 4), but they contain accumulated magnetite (up to 5–7 vol%) and abundant rafts of plagioclase and clinopyroxene (Table 1). They also have large positive whole-rock Eu anomalies indicating they may have assimilated plagioclase-rich rocks and/or accumulated plagioclase. Early to late monzonite porphyry dikes crosscut the biotite pyroxenite cumulate rocks, and some late monzonite porphyry dikes locally crosscut associated magmatic-hydrothermal diatreme breccias. Some late monzonite porphyries contain rare titanite (Table 1) and have whole-rock Eu anomalies that change from small negative anomalies to positive anomalies with magmatic differentiation. This change is also observed during differentiation from Kaskanak granodiorite to the most evolved granite porphyry (Fig. 8).

The bulk of the Kaskanak batholith is calc-alkaline granodiorite in composition with volumetrically minor amounts of porphyritic andesite dikes and a series of more differentiated granodiorite to

granite porphyry dikes (Olson 2015). The porphyritic andesite dikes and granodiorite of the Kaskanak batholith have 56–67 wt% SiO₂ and overlap in major and trace element compositions with alkalic suite having the same SiO₂ contents. Many of the porphyritic andesite dikes occur along the flanks of the Kaskanak batholith and have been weakly affected by sodic-calcic alteration resulting in reduced alkalis and LILE (Fig. 6). A sample of porphyritic andesite in the 1 Gold Zone contains the lowest SiO₂ and was chosen as a potential parental magma for purposes of modeling the Kaskanak batholith magmatic evolution (discussed later). The more silicic and younger Kaskanak granodiorite and granite porphyry dikes (67–77 wt% SiO₂) lie along the same trends in variation and spider diagrams, but are evolved to lower transition metal (Mg, Fe, Cr, Sc), HFSE, and REE concentrations (Figs. 6, 7, and 8). The most differentiated granite porphyry dikes are REE-poor, have a pronounced concave upward chondrite-normalized REE profile, and have a range from no Eu anomaly to a moderate positive Eu anomaly in the most silicic compositions (Fig. 8). For all the Kaskanak batholith intrusions, Sr/Y ratios range from 20–65 (from volcanic arc to adakitic composition) and La/Yb ratios range from 4–16 (normal volcanic arc) with the highly evolved porphyries having the highest ratios; note that Sr has been significantly depleted in many hydrothermally altered samples, which are excluded from the reported Sr/Y ratios (Fig. 7). The V concentrations and V/Sc

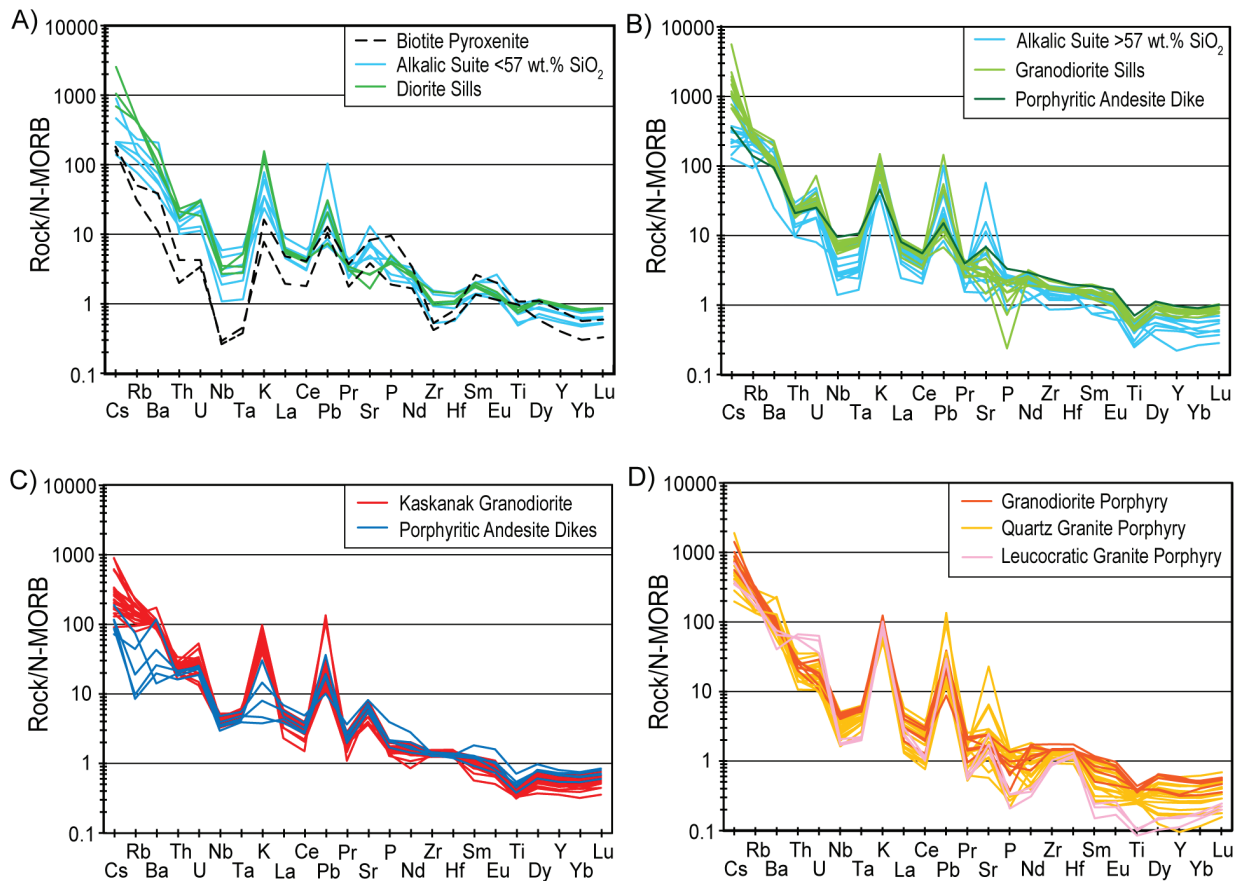


FIGURE 6. Trace element spider diagrams for Late Cretaceous igneous rocks of the Pebble district normalized to N-MORB (Sun and McDonough 1989). **(a)** Early alkalic and calc-alkalic <57 wt% SiO₂; **(b)** early alkalic and calc-alkalic >57 wt% SiO₂; **(c)** Kaskanak granodiorite and porphyritic andesite dikes; **(d)** granodiorite and granite porphyries of the Kaskanak batholith.

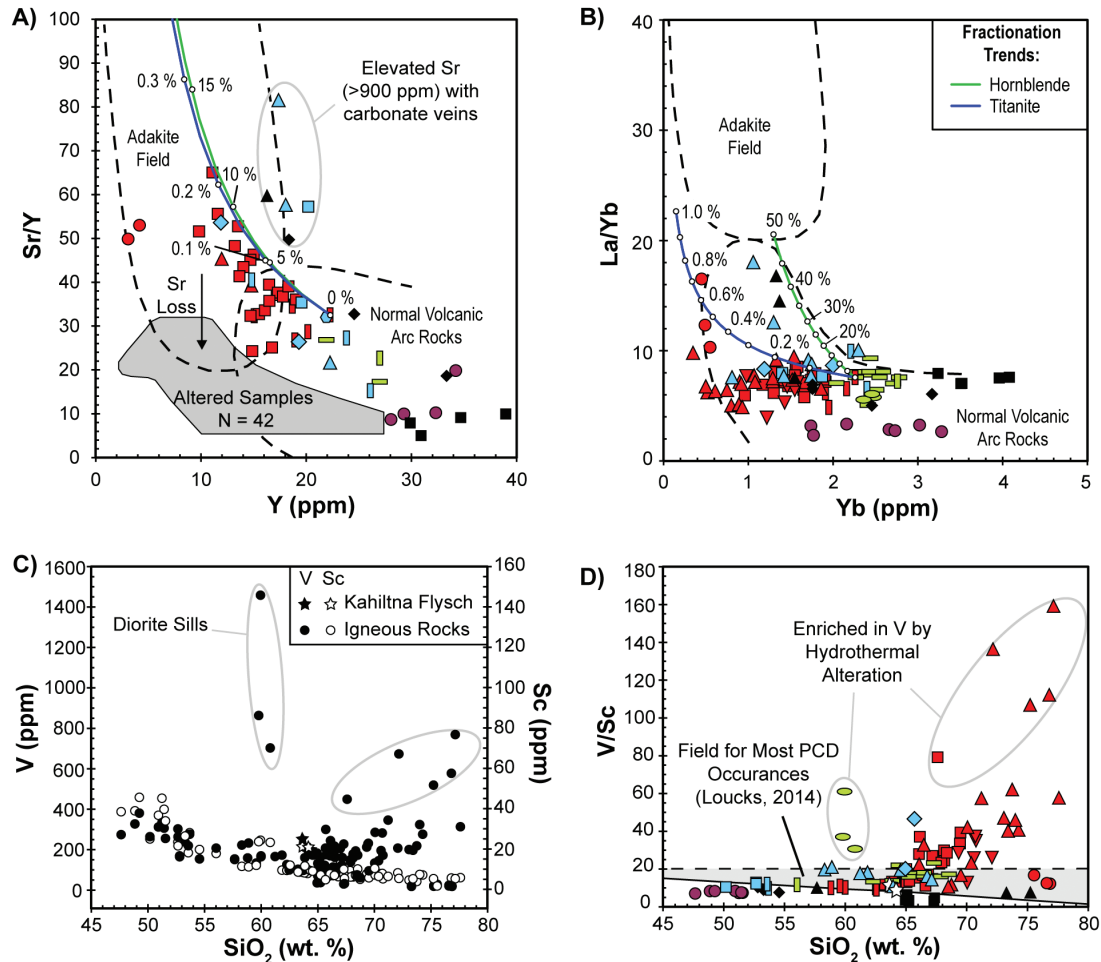


FIGURE 7. Rayleigh fractionation models for crystallization of 0 to 50 wt% hornblende (green line) and 0 to 1.0 wt% for titanite (blue line) illustrated on plots (a) Sr/Y vs. Y and (b) La/Yb vs. Yb. The model uses the porphyritic andesite dike starting compositions and partition coefficients listed in Tables¹ 3 and 4. Note that most porphyry intrusions are somewhat hydrothermally altered and have low-Sr/Y ratios as a result of likely Sr loss. Nonetheless, the freshest samples have Sr/Y < 65 and lie in both the adakitic and normal arc fields of Richards and Kerrich (2007). Vanadium and scandium behaviors depart from one another as illustrated in (c) V and Sc vs. SiO₂, and (d) V/Sc vs. SiO₂. Vanadium has incompatible behavior at elevated silica likely because of V⁴⁺ and V⁵⁺ formed under highly oxidized magmatic conditions (see text for details). The elevated V concentrations of circled samples may likely be due to hydrothermal enrichment. Symbols as in Figure 4 or as labeled.

ratios of samples of the Kaskanak batholith are also highly elevated especially in the most evolved samples. The V/Sc ratios are much higher than typical porphyry copper magmas reported by Loucks (2014). Furthermore, the most leucocratic granite porphyries are highly enriched in some incompatible LILEs such as U, Th, and Rb, and strongly depleted in Ti compared to less evolved granodiorite and quartz granite porphyry intrusions (Figs. 5 and 6). The highly elevated LILEs in these leucocratic granites may be a product of late-stage filter-pressing or late-stage crystallization of segregated pockets of melt near the solidus.

Paleocene–Eocene igneous rocks. Igneous rocks associated with the Talarik Formation and the Koktuli Volcanics and associated plutonic rocks are metaluminous, calc-alkaline rocks with SiO₂ concentrations that range from 53–76 wt% SiO₂. These rocks have depletions in Nb, Ta, and Ti concentrations similar to Late Cretaceous igneous rocks. They have elevated concentrations of Th, U, and REE relative to most Late Cretaceous intrusions (Fig. 5). The

Mg, Sc, Ni, and Cr concentrations in the basaltic andesites are also relatively depleted compared to the gabbro and basalt roof pendants. Phenocryst-poor Paleocene dacite dikes that crosscut mineralization in the East Zone are strongly depleted in MREEs and have elevated Sr/Y and La/Yb ratios similar to some of the most differentiated Late Cretaceous intrusions including monzonite porphyry and leucocratic granite porphyry dikes (Fig. 7). The V/Sc ratios for all Paleocene and Eocene igneous rocks generally are <10 and fall outside the field of most porphyry deposit intrusions (Fig. 7).

Radiogenic isotopes

The Sr and Nd isotopic data from this study include 1 sample from a gabbro roof pendant, 10 samples from Late Cretaceous intrusions, and 1 sample from a Paleocene andesite dike (Table 2). Initial ⁸⁷Sr/⁸⁶Sr and ¹⁴³Nd/¹⁴⁴Nd ratios were calculated at 180, 90, and 65 Ma, respectively, and are compared to other Sr and Nd isotopic data for Late Cretaceous and Paleocene igneous rocks

from the Pebble deposit (Fig. 9; Ayuso et al. 2013; Goldfarb et al. 2013). Initial $^{87}\text{Sr}/^{86}\text{Sr}$ and $^{143}\text{Nd}/^{144}\text{Nd}$ isotopic compositions of all rocks from this study have a range of 0.70329–0.70424 and 0.51270–0.51284 ($\epsilon\text{Nd}_i = +4.4$ to $+6.1$), respectively, and where other data are included, the total range is 0.70329–0.70554 and 0.51257–0.51287 ($\epsilon\text{Nd}_i = +1.0$ to $+6.3$), respectively.

The data are broadly comparable, however, Ayuso et al. (2013) reported ϵNd_i values for Cretaceous rocks ($\epsilon\text{Nd}_i = +1.0$ to $+4.5$) that are mostly lower than the ϵNd_i values from Goldfarb et al. (2013) and this study combined ($n = 20$, $\epsilon\text{Nd}_i = +4.4$ to $+6.3$). Photos of several samples of drill core analyzed by Ayuso et al. (2013) contain xenoliths of the Kahiltna flysch ($\epsilon\text{Nd}_i = -1$ to -5 ; Aleinikoff et al. 2000). Inclusion of the Kahiltna flysch clasts in analyzed samples or local melting of the Kahiltna flysch by Pebble intrusions would both result in anomalously low- ϵNd_i values such as those reported by Ayuso et al. (2013).

Subdividing the total data set of igneous rocks at Pebble into Jurassic, Cretaceous, and Paleocene/Eocene subsets ($^{87}\text{Sr}/^{86}\text{Sr}_i$ ratios = 0.70338, 0.70329–0.70467, 0.70348–0.70354, respectively; $^{143}\text{Nd}/^{144}\text{Nd}_i$ ratios = 0.51270, 0.51257–0.51284, 0.51274–0.51287, respectively; and ϵNd_i values = 5.7, 1.0–6.3, 3.7–6.2, respectively), the least radiogenic isotopic compositions all overlap suggesting little change of the isotopic composition of melts from the source

region with time. The isotopic spread toward more radiogenic values is apparently from variable amounts of assimilation of the Kahiltna flysch, the only radiogenic source identified in the region.

Trace element concentrations in zircon and titanite

Zircons that grow from arc magmas have very low LREE and strongly elevated HREE concentrations with distinctive positive Ce and negative Eu anomalies (Figs. 10 and 11). Zircons that grow from mineralized intrusions are typically characterized by larger positive Ce anomalies and smaller negative Eu anomalies than barren intrusions, which reflect the elevated magmatic oxidation states ($\Delta\text{NNO}+1$ to $+3$) in the mineralizing intrusions (Ballard et al. 2002; Dilles et al. 2015). Additionally, small Eu anomalies may be accentuated by the suppression of plagioclase crystallization in hydrous melts (Ballard et al. 2002; Hoskin and Schaltegger 2003; Trail et al. 2011; Dilles et al. 2015). Extensive amphibole, pyroxene, or minor titanite fractionation may also increase the Yb/Gd ratio of the melt (Kay and Mpodozis 2001; Richards and Kerrich 2007) and thus increase the Yb/Gd ratio of late crystallizing zircon.

Zircons trace elements from intrusions in the Pebble district are plotted in Figure 10. Zircons from the diorite sills and Koktuli Mountain granodiorite have very low-Eu/Eu* values (mostly

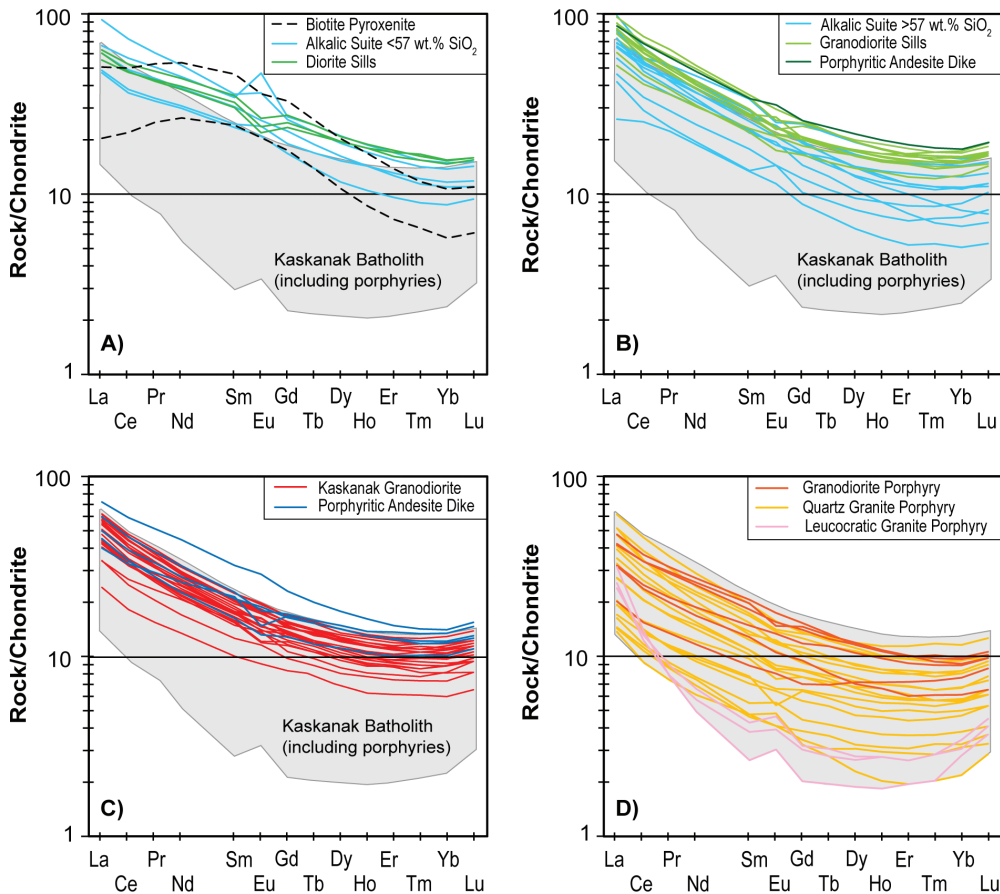
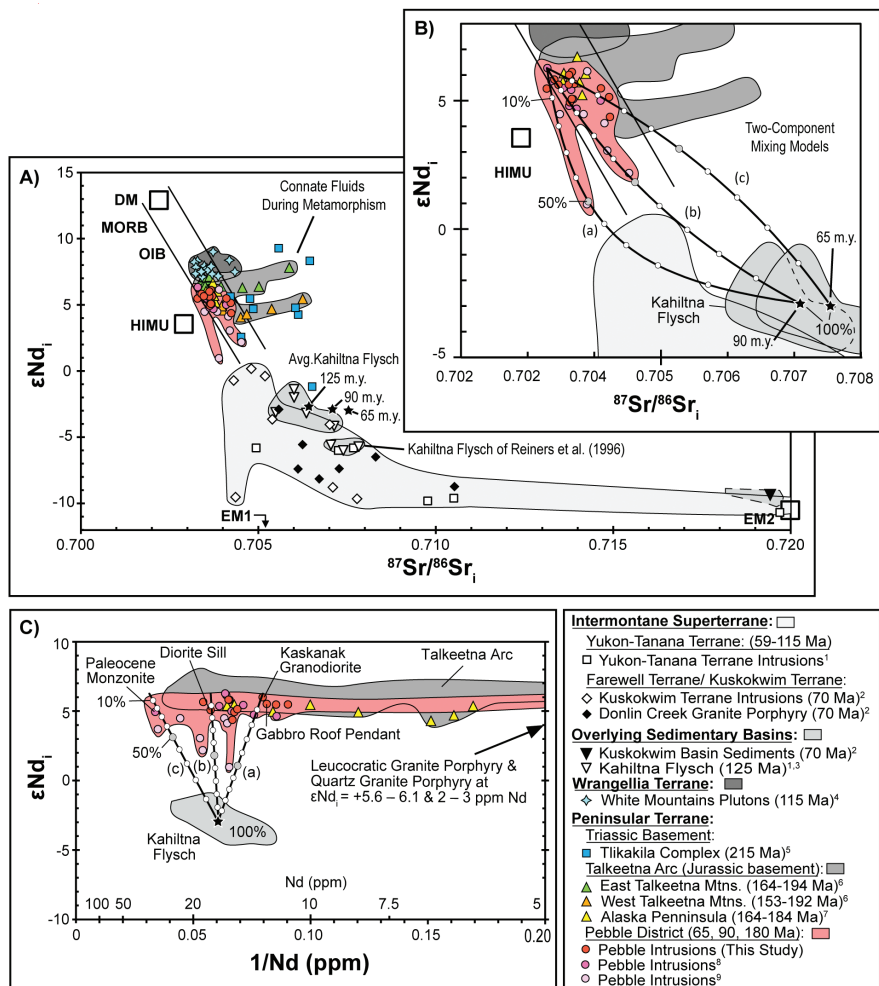


FIGURE 8. Rare earth element spider diagrams for Late Cretaceous igneous rocks of the Pebble district normalized to chondrite (McDonough and Sun 1995). (a) Early alkalic and calc-alkalic <57 wt% SiO₂; (b) early alkalic and calc-alkalic >57 wt% SiO₂; (c) Kaskanak granodiorite and porphyritic andesite dikes; (d) granodiorite and granite porphyries of the Kaskanak batholith.

FIGURE 9. (a) Sr and Nd isotopic compositions of Mesozoic and Paleocene rocks in terranes of southern Alaska. Note the isotopic composition of the Kahiltna flysch reported by Reiners et al. (1996) is slightly more radiogenic and was not utilized in the modeling. (b) Enlargement of Sr-Nd isotopic data illustrating two-component mixing models of mean (in 10 wt% increments) Kahiltna flysch with a primitive composition of Kaskanak granodiorite (a), diorite sills (b), and Paleocene monzonite porphyry (c). See text for rock compositions. (c) ϵ_{Nd_i} vs. $1/\text{Nd}$ for the two-component mixing models. Mixing models suggest the Kaskanak granodiorite assimilated ≤ 10 wt% of the Kahiltna flysch, whereas other Late Cretaceous intrusions assimilated ≤ 20 wt% Kahiltna flysch. Data from Table 2 and the following: (1) Aleinikoff et al. (2000), (2) Goldfarb et al. (2004), (3) Reiners et al. (1996), (4) Snyder and Hart (2007), (5) Amato et al. (2007a), (6) Rioux et al. (2007), (7) Rioux et al. (2010), (8) Goldfarb et al. (2013), and (9) Ayuso et al. (2013).



≤ 0.3), low-Ce/Nd ratios (≤ 22), and low-Yb/Gd ratios (≤ 18) suggesting significant plagioclase-dominated fractionation, and are the least prospective in terms of porphyry copper fertility. Zircons from the alkalic monzonite porphyry appear to be spread toward lower temperatures with lower recorded concentrations of Hf and elevated Ce/Nd ratios. A possible contaminant could be the calc-alkaline granodiorite sills, but no definitive field evidence has documented magma mingling of these intrusions. The granodiorite sills, like the Kaskanak batholith, have lower temperature zircons, elevated Yb/Gd ratios (26–54), very high-Eu/Eu* anomalies (0.7–1.1), and very high-Ce/Nd ratios (up to 126), and thus have a very fertile zircon trace element signature. No known mineralization is associated with the granodiorite sills, which may be a result of volatile loss coeval with the formation of large diatreme breccias (Figs. 2 and 3). Other barren Paleocene andesite and dacite dikes also have perspective Eu anomalies (0.6–1.0), but have moderate Ce/Nd ratios (7–53) and lower Yb/Gd ratios (16–33). All intrusions of the mineralized Kaskanak batholith have fertile zircon trace element signatures with high Eu/Eu* values (0.4–1.1), high Ce/Nd ratios (up to 152), and elevated Yb/Gd ratios (13–56) owing to extensive fractionation of amphibole and titanite under hydrous and oxidized magmatic conditions.

Titanite in the Pebble district is present in all phases of the Kaskanak batholith and occurs sparsely in some of the unaltered samples of monzonite porphyries of the alkalic suite. Outside the hydrothermal footprint, the Kaskanak granodiorite contains abundant titanite (0.5–2.0 vol%) and ubiquitous, but minor zircon (<0.05 vol%). Titanite contains high concentrations of REE and HFSE (Y, Zr, Hf, Nb, Ta, Th, and U), and titanite analyzed from the Kaskanak granodiorite contains >100 times more REE and 10–100 times more HFSE than whole-rock compositions (Fig. 11g, Appendix 1D). Because of the abundance of titanite and its high concentrations of HFSE and REE, mass balance dictates that the vast majority of the whole-rock HFSE and REE content resides in titanite.

The REE and HSFE contents of unaltered titanites are normally zoned and decrease from core to rim sympathetic with Y decrease from 6000 to 2000 ppm (Fig. 12). Generally, titanite chondrite-normalized REE patterns range from convex “seagull-shaped” to concave “U-shaped” profiles (e.g., $\text{Dy}_{\text{CN}}/\text{Yb}_{\text{CN}} < 1$; Figs. 11c and 12f). This observed preferential depletion of middle REE relative to light and heavy REE is due to the larger partition coefficients for the middle REE compared to light and heavy REE (Table 1; Bachmann et al.

TABLE 2. Sr-Nd isotopic compositions

Sample ID	Lithology	Age ^a (Ma)	Rb ^b (ppm)	Sr ^b (ppm)	⁸⁷ Sr/ ⁸⁶ Sr ^c	2σ	Calc ⁸⁷ Rb/ ⁸⁶ Sr	⁸⁷ Sr/ ⁸⁶ Sr ^d	Sm ^b (ppm)	Nd ^b (ppm)
GH12-314-103	Gabbro	~180	19.9	201	0.704109	18	0.2863	0.703377	3.68	12.29
3121-1080	Diorite Sill	98.1	238.3	238	0.707368	17	2.8968	0.703668	4.46	17.42
GH12-312-42.5	Monzonite Ppy	~95	52.6	212	0.705019	18	0.7177	0.704103	2.62	11.06
10478-515	Monzonite Ppy	~96	146.6	103	0.708666	19	4.1184	0.703406	3.22	15.37
3082-862	Monzonite Ppy w/megacrystic K-feldspar	94.9	169.2	510	0.704864	20	0.9596	0.703638	3.37	14.81
7375-3310	Granodiorite Sill	94.9	171.6	592	0.704777	18	0.8384	0.703706	4.11	18.43
10500-650.5	Andesite Ppy	91.1	10.5	579	0.704293	16	0.0525	0.704226	3.36	14.53
11528-1412	Kaskanak Granodiorite	91.0	43.4	650	0.703874	17	0.1931	0.703628	2.89	12.56
7385-2410	Granodiorite Ppy	90.3	144.3	141	0.707071	17	2.9608	0.703290	2.91	11.72
8443-1978	Quartz Granite Ppy	88.9	115.7	101	0.707853	15	3.3144	0.703620	0.68	3.13
2047-778	Leucocratic Granitic Ppy	89.2	116	154	0.706450	16	2.1791	0.703667	0.39	2.24
7385-2821	Paleocene Andesite Dike	64.0	44.5	965	0.704362	15	0.1334	0.704239	3.60	14.99

^a For U-Pb ages and uncertainties, see Olson (2015). Estimated ages (~) are based on ages reported for similar intrusions.

^b Compositions determined by ICP-MS at Washington State University.

^c Measured ⁸⁷Sr/⁸⁶Sr were corrected for Rb interference, mass fractionation (using ⁸⁶Sr/⁸⁸Sr = 0.1194), and internally standardized to NIST SRM987 at the University of Cape Town, South Africa (Miková and Denková, 2007). Measured ¹⁴³Nd/¹⁴⁴Nd ratios were corrected for Sm and Ce interferences, mass fractionation (using ¹⁴⁰Nd/¹⁴⁴Nd = 0.7219), and internally standardized to JNd-1 (Tanaka et al. 2000). An external USGS basalt standard, BHVO-2, was analyzed twice as an unknown yielding values of 0.703472 and 0.703495 for ⁸⁷Sr/⁸⁶Sr, and 0.512987 and 0.512997 for ¹⁴⁶Nd/¹⁴⁴Nd, which fall within reported uncertainty for the standard (0.703479 ± 20; 0.512984 ± 15; Weis et al. 2006). Reported 2σ uncertainties correspond to the last two significant digits of the measured ratios.

^d Initial ⁸⁷Sr/⁸⁶Sr and ¹⁴³Nd/¹⁴⁴Nd ratios were calculated for an age of *t* = 90 m.y., except for the gabbro (*t* = 180 m.y.) and a Paleocene andesite (*t* = 65 m.y.).

(Table extends to next page)

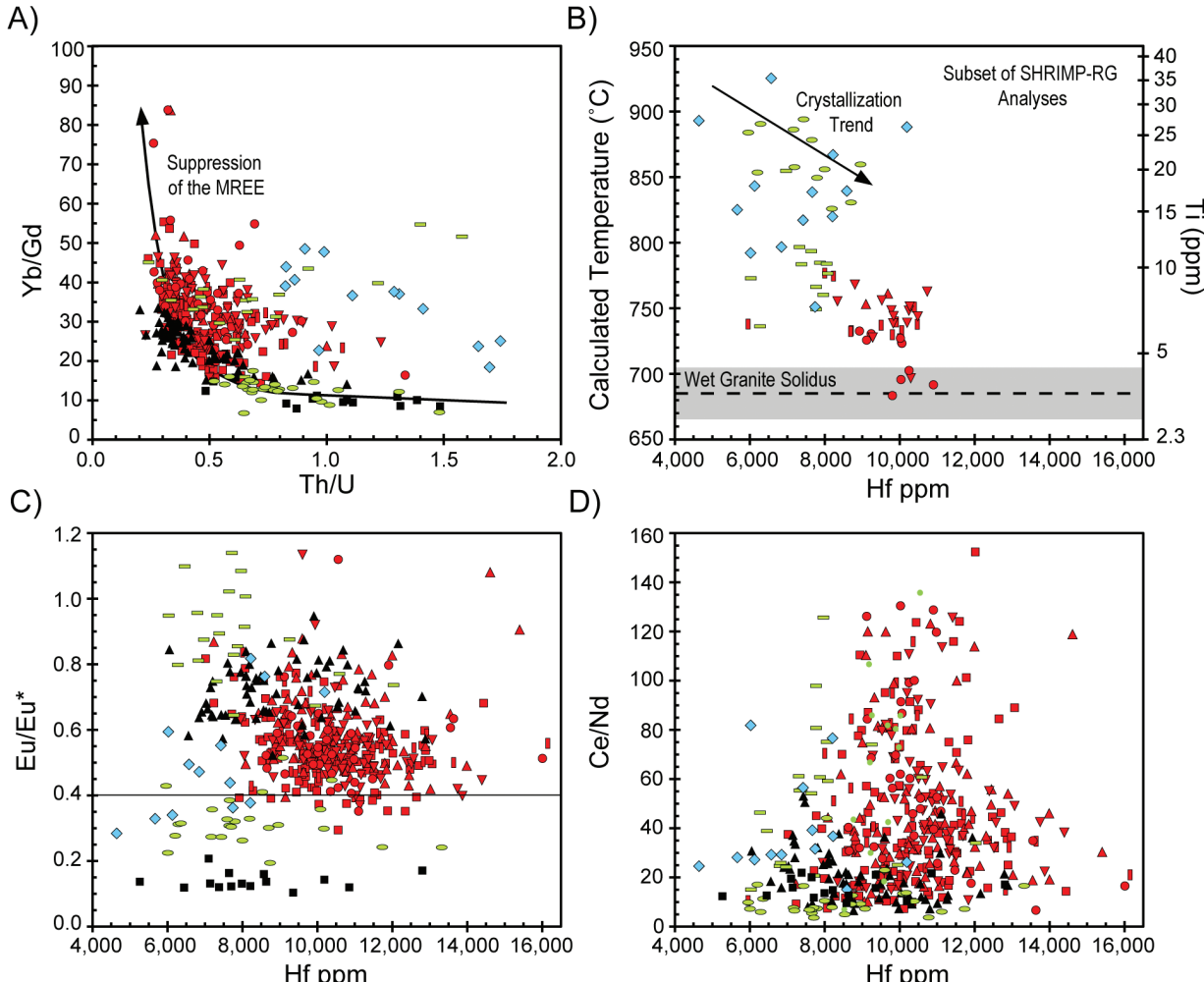


FIGURE 10. Zircon trace element data from LA-ICP-MS and SHRIMP-RG analyses. (a) Yb/Gd vs. Th/U demonstrating suppression of the MREE with crystallization. (b) Ti-in-zircon temperatures vs. Hf using the formulation of Ferry and Watson (2007). (c) Eu anomaly vs. Hf, and (d) Ce/Nd vs. Hf. Eu/Eu* anomalies ≥0.4 are characteristic of most porphyry copper deposit occurrences (Ballard et al. 2002; Dilles et al. 2015). Symbols as in Figure 4.

TABLE 2. —EXTENDED

Sample ID	$^{143}\text{Nd}/^{144}\text{Nd}^c$	2σ	Calc $^{147}\text{Sm}/^{144}\text{Nd}$	$^{143}\text{Nd}/^{144}\text{Nd}_i^d$	ϵNd_i
GH12-314-103	0.512909	12	0.1810	0.512696	5.65
3121-1080	0.512873	12	0.1547	0.512782	5.07
GH12-312-42.5	0.512887	14	0.1432	0.512803	5.48
10478-515	0.512895	13	0.1266	0.512820	5.82
3082-862	0.512856	12	0.1375	0.512775	4.93
7375-3310	0.512891	13	0.1348	0.512812	5.65
10500-650.5	0.512868	12	0.1398	0.512785	5.13
11528-1412	0.512911	14	0.1391	0.512830	6.00
7385-2410	0.512891	15	0.1501	0.512802	5.47
8443-1978	0.512887	13	0.1313	0.512810	5.62
2047-778	0.512898	14	0.1052	0.512836	6.12
7385-2821	0.512840	14	0.1451	0.512778	4.37

2005; Colombini et al. 2011). At low-Y contents of 300 to 2000 ppm, the REE and HFSE content and Zr-in-titanite temperature vary broadly (Fig. 12), as described above, and are not well correlated with Y content. For example, Nb and Th strongly decrease sympathetic with the decrease of Y from early titanite cores to rims presumably as a result of titanite removing these elements from the melt, but increase sharply in some late cores and rims. These late cores and rims have relatively high Nb, Th, Nb/Ta, and Zr-in-titanite temperatures (Fig. 12). Some of these analyses correspond with observed titanite resorption features and rim overgrowths (Fig. 11a).

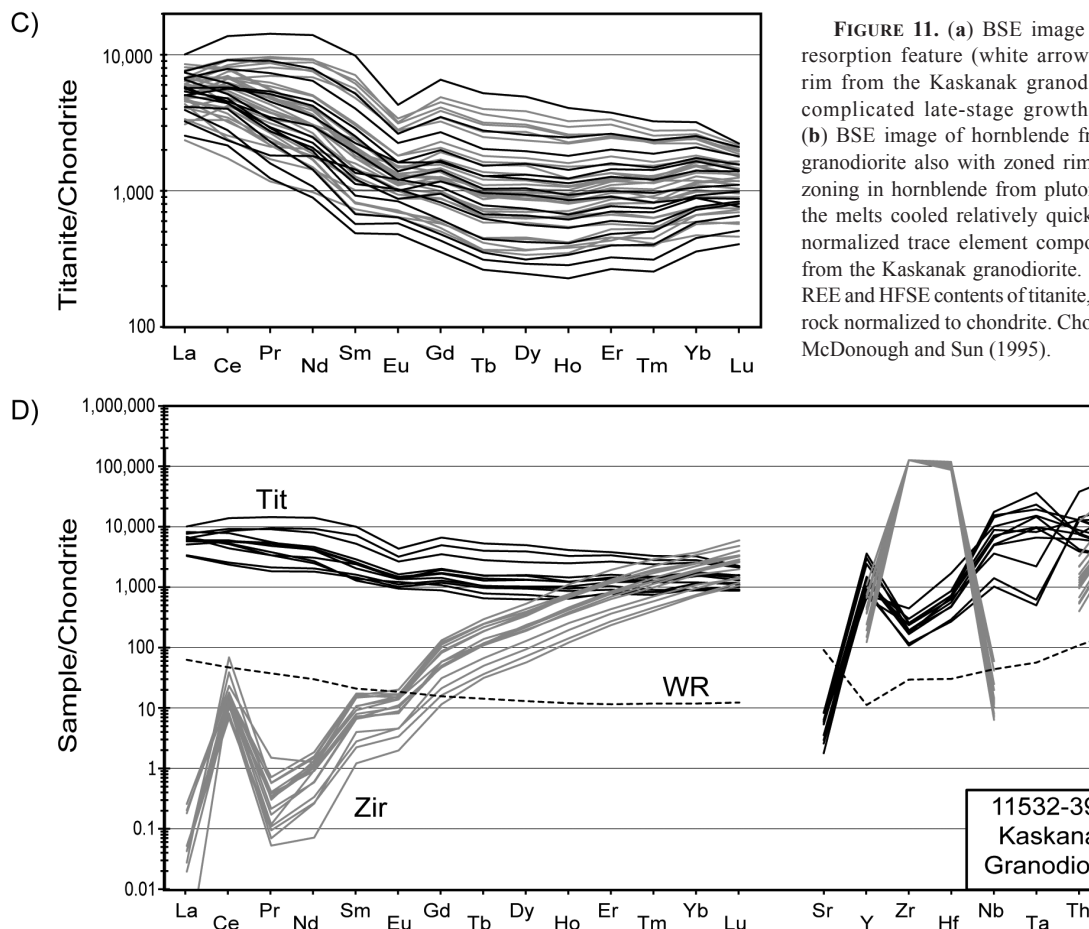
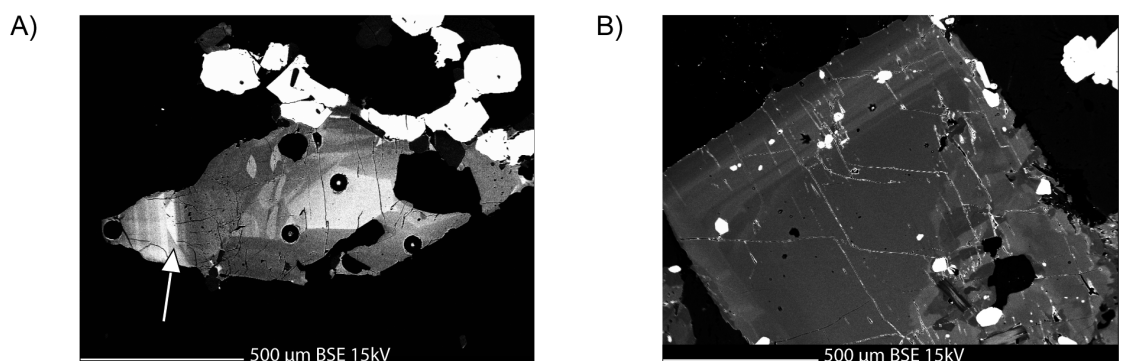


FIGURE 11. (a) BSE image of titanite with a resorption feature (white arrow) and overgrowth rim from the Kaskanak granodiorite implicating complicated late-stage growth of titanite rims. (b) BSE image of hornblende from the Kaskanak granodiorite also with zoned rims. Preservation of zoning in hornblende from plutonic rocks suggests the melts cooled relatively quickly. (c) Chondrite-normalized trace element compositions of titanite from the Kaskanak granodiorite. (d) Representative REE and HFSE contents of titanite, zircon, and whole-rock normalized to chondrite. Chondrite values from McDonough and Sun (1995).

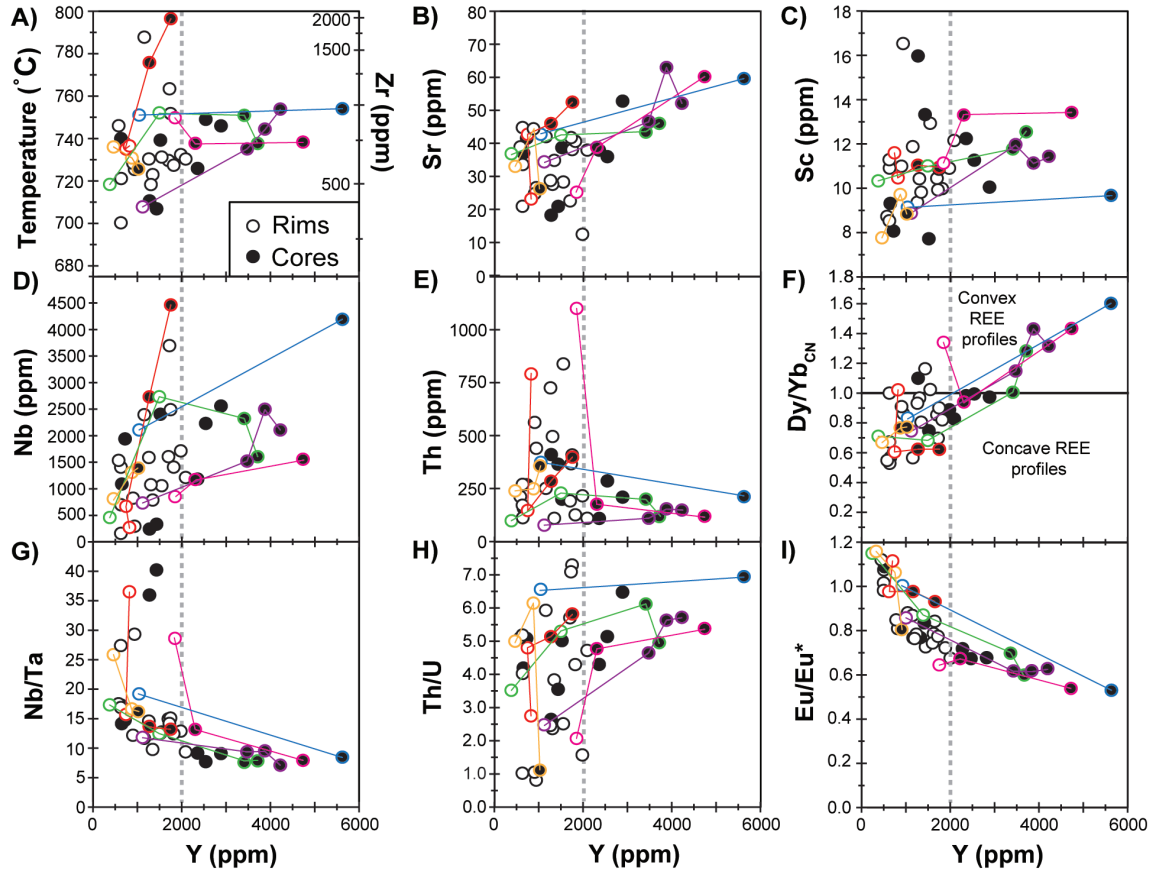


FIGURE 12. Trace element compositions of titanite rims and cores from the unaltered Kaskanak granodiorite. Colored tie-lines indicate core to rim analyses on selected titanite grains. Large variations of trace element contents and ratios at ≤ 2000 ppm Y are correlated with a large range of Zr-in-titanite temperatures from 700–800 °C. Because of the affinity of titanite to incorporate large amounts of REE and HFSEs, the concentration of these elements is expected to decrease in melts with titanite crystallization. Dashed gray lines at 2000 ppm Y indicate the lower limit of the normal crystallization and crystal-fractionation processes where trace elements vary smoothly with Y. In comparison, complex late-stage processes at Y ≤ 2000 ppm include irregular and large variations in Nb/Ta, Th/U, Dy/Yb, and locally high concentrations of Sc, Nb, Th, U, and REE. Note that Eu/Eu* increases steadily as Y decreases from 6000 to 500 ppm.

Ti-in-zircon and Zr-in-titanite temperatures

Ti-in-zircon and Zr-in-titanite temperatures of Late Cretaceous rocks are calculated and plotted in Figures 10b and 12a. The calculations assume activities of TiO₂ and SiO₂ of 0.7 and 1.0, respectively; and titanite crystallization pressure of 0.2 GPa for the Kaskanak batholith (see Methods for further details). The results of Ti-in-zircon temperature estimates for Late Cretaceous pre-mineral diorite sills, monzonite porphyries, and granodiorite sills are all relatively hot (930–730 °C; Fig. 10b). For the younger Kaskanak batholith intrusions, Ti-in-zircon and Zr-in-titanite temperature estimates are in agreement (Figs. 10b and 12a) and suggest zircon and titanite crystallized together at lower magmatic temperatures (760–680 °C). Some titanite cores and many titanite rim analyses, however, reflect higher temperatures (up to 800 °C) at relatively low-Y and REE concentrations (Fig. 12) and record anomalous trace element compositional variance, reflecting complicated late-stage magmatic processes correlated with fluctuations in temperature.

Trace elements of inherited zircons

Inherited zircons are relatively abundant in Late Cretaceous intrusions in the district, especially in the early monzonite porphyries of the alkalic suite (commonly >95% inheritance) and the diorite and granodiorite sills (commonly >50% inheritance). The histograms of inherited zircons indicate that Cretaceous ages dominate with progressively fewer Jurassic and Triassic ages, and 12% Paleozoic ages as old as Cambrian (Fig. 13b). All inherited zircons exhibit normal oscillatory zoning textures, elevated Th/U ratios (e.g., ≥ 0.4), and REE abundances consistent with an original igneous source. The maximum values of Eu/Eu*, Yb/Gd, and Ce/Nd occur < 200 Ma during the Jurassic–Cretaceous periods (Figs. 13c–13e). In contrast, the most reduced values occur in the Permian to Triassic periods from ~ 300 to 200 Ma (Figs. 13d–13e) consistent with timing of late Skolai arc magmatism (~ 290 –320 Ma; Fig. 1) and the Nikolai greenstone flood basalts (~ 240 –250 Ma) within the Wrangellia terrane (Beard and Barker 1989). Pennsylvanian to Cambrian inheritance has slightly larger Eu/Eu* and Ce/Nd values, and much larger Yb/Gd ratios. Apart

from the Skolai arc intrusions, the sources for many of these older zircons are unknown, and their trace element composition suggests derivation from more oxidized and fractionated melts than the Permian to Triassic zircons.

DISCUSSION

The geochemical composition of Late Cretaceous magmatic arc rocks that developed after suturing of the WCT to the North American continental margin in the Iliamna region is more evolved than the older pre- to syn-collisional Jurassic Talkeetna Arc basement rocks. Late Cretaceous to Eocene intrusive rocks are alkaline to high-K calc-alkaline with elevated LILEs and HFSEs compared to the Talkeetna Arc magmatic rocks that range from tholeiitic to calc-alkaline compositions (Greene et al. 2006). Late Cretaceous intrusions have a larger range of La/Yb and Sr/Y ratios (La/Yb = 5–18; Sr/Y = 20–55) compared to the Talkeetna Arc volcanic rocks (La/Yb = 2–5; Sr/Y = 3–30; Clift et al. 2005). Sr/Y ratios of Late Cretaceous intrusions overlap the adakite field (Fig. 7a), but Late Cretaceous and Jurassic magmatic rocks both lack adakite-like La/Yb ratios >20 (Fig. 7b; Richards and Kerrich 2007). Late Cretaceous to Eocene igneous rocks also have large arc-like depletions in Nb, Ta, and Ti compared to the Talkeetna Arc volcanic rocks. These depletions become more

pronounced with arc maturation consistent with the findings of Amato et al. (2007b). In sharp contrast, Pebble gabbro and basalt roof pendants, inferred to be Jurassic in age, lack these depletions. Chondrite-normalized REE profiles and low-La/Yb ratios of all regional intrusions are consistent with volcanic arc magmatism developed in a relatively thin crust where heavy REE-rich garnet was not stable. Residual garnet or garnet fractionation would significantly increase the observed La/Yb and Sr/Y ratios if present (Kay and Mpodozis 2001). The crustal thickness during Cretaceous to Eocene magmatism is unknown, but likely is similar or less than the modern crustal thickness estimate of 30 km for the Iliamna Quadrangle based on gravity surveys (Barnes 1977) and therefore crustal garnet would be unlikely. The most primitive Late Cretaceous igneous rocks exposed in the region are shoshonite to andesite in composition (Fig. 4), similar to other arc suites developed in thin crust. These rocks likely originated via hybridization of mantle-derived and lower crustal melts (Hildreth and Moorbat 1988; Annen et al. 2006). The most mafic Paleocene and Eocene magmatic rocks share a similar range from differentiated basaltic andesite to andesite, but are locally all calc-alkaline in composition. In contrast, mafic end-members of the Jurassic Talkeetna Arc commonly contain more abundant primitive basalts, gabbros, and gabbronorites

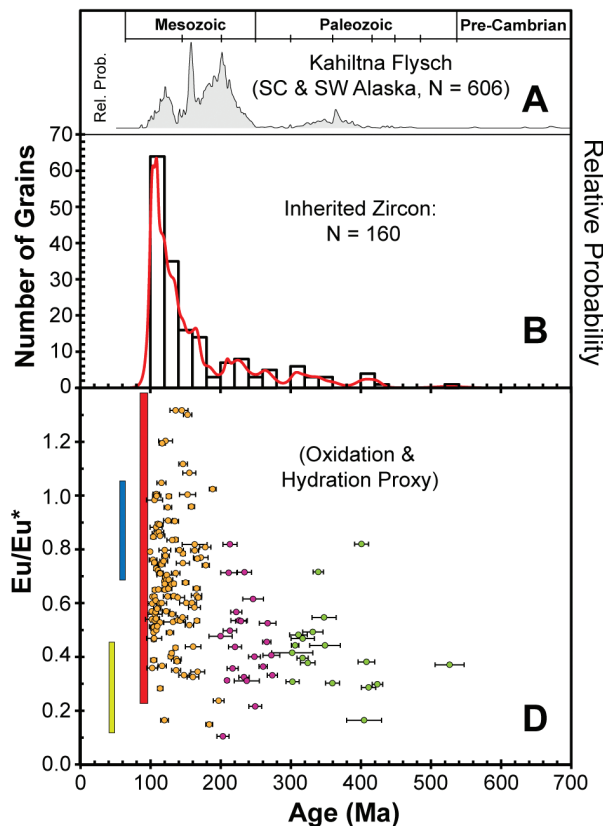
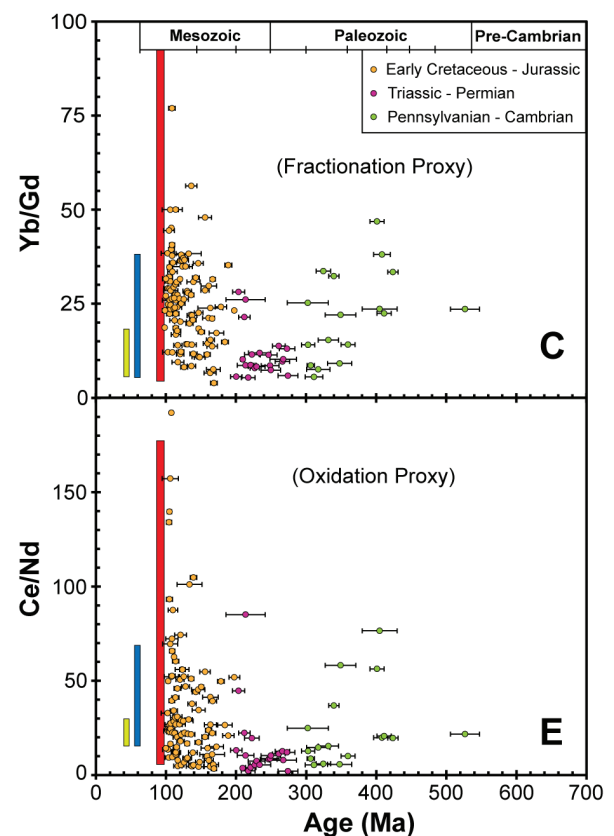


FIGURE 13. Age and rare earth element compositions of inherited zircons from Late Cretaceous intrusions in the Pebble district. **(a)** Relative probability distribution of detrital zircons from the Kahiltna Flysch in south-central and southwestern Alaska (from Hampton et al. 2010). **(b)** Relative probability and histogram of inherited grain ages from Cretaceous igneous rocks in the Pebble district. **(c)** Yb/Gd vs. age, **(d)** Eu/Eu^{*}_{CN} vs. age, and **(e)** Ce/Nd vs. age of inherited zircons from Cretaceous igneous rocks in the Pebble district. The range of Cretaceous zircons (red box), Paleocene zircons (blue box), and Eocene zircons (green box) from Figure 10 are shown for comparison. All grain ages shown at 2 σ uncertainty.



(Detterman and Reed 1980; DeBari and Sleep 1991; Nokleberg et al. 1994; Clift et al. 2005; Greene et al. 2006). Nonetheless, the primitive Talkeetna arc magmas were contaminated by some older crustal components on the basis of slightly radiogenic initial Sr and Nd isotopes (Fig. 9), and inherited Paleozoic zircons in both the West Talkeetna Mountains and the Alaska Peninsula (Clift et al. 2005; Greene et al. 2006; Rioux et al. 2007, 2010). In comparison, the Pebble Late Cretaceous intrusions may have also assimilated older Paleozoic crust from the roots of the Peninsular terrane, but also variably assimilated the Late Jurassic–Early Cretaceous Kahiltna flysch and possibly some Jurassic arc basement rocks on basis of inherited zircons and Sr and Nd isotopes.

Source region and crustal assimilation

The magnitude of crustal assimilation by Late Cretaceous intrusions is difficult to constrain without context for possible sources. Inherited (xenocrystic) zircons provide a robust line of evidence for crustal assimilation and provide evidence for the age of unexposed basement rocks in the region. Most of the inherited zircons in Late Cretaceous intrusions in the Pebble district are likely sourced from the Kahiltna flysch. However, some monzonite porphyry intrusions contain predominantly Early Devonian–Pennsylvanian xenocrystic zircons that suggest contributions from basement rocks. The lack of inherited Proterozoic zircons rules out contributions from the Intermontane superterrane and restricts inherited zircons to a WCT origin. Nonetheless, anomalous Proterozoic and few Archean zircons have been found east of Lake Clark in detritus associated with the Tlikakila Complex (Amato et al. 2007a) and within xenoliths in Mount Redoubt volcanic rocks (Bacon et al. 2012). Possible sources of recycled Paleozoic zircons within the Peninsular terrane in SW Alaska include Paleozoic pelitic and quartz-mica schists, which are discontinuously exposed as roof pendants in Triassic and younger plutons between the southern margins of the Western Alaska Range (Csejtey et al. 1978; Nokleberg et al. 1994; Amato et al. 2007c) and north side of the Border Ranges fault system (Nokleberg et al. 1994). Some Pennsylvanian to Early Permian zircons may be derived from Skolai Arc plutons (Aleinikoff et al. 1988; Gardener et al. 1988; Beard and Barker 1989) that are exposed to the east in the Wrangellia and Alexander terranes of the Talkeetna and East Alaska ranges (Fig. 1). Nonetheless, Skolai Arc plutons may form basement that underlies the Kahiltna flysch in the SW Alaska Range as indicated by Pennsylvanian gabbroic xenoliths in volcanic rocks from Mt. Redoubt (Fig. 1; Bacon et al. 2012). Inherited Paleozoic zircons are also reported from Jurassic plutonic rocks along the Alaska Peninsula (Amato et al. 2007a), volcanic tuffs of the Kamishak and Talkeetna Formations (Pálfy et al. 1999), and in some Jurassic plutons in the Western Talkeetna Mountains (Rioux et al. 2007).

Sr and Nd isotopic ratios are generally primitive and restricted in range for melts throughout the WCT due to its youth and overall primitive composition relative to average continental crust. Nonetheless, some Jurassic and older basement rocks have slightly elevated Sr isotopic ratios exhibiting initial $^{87}\text{Sr}/^{86}\text{Sr} > 0.7050$ (Fig. 9) that are likely caused by metasomatic alteration by connate fluids during greenschist facies metamorphism in

the WCT (Detterman and Reed 1980; Nokleberg et al. 1994; Wallace et al. 1989; Amato et al. 2007a). In contrast, initial $^{87}\text{Sr}/^{86}\text{Sr}$ ratio ranges of 0.70329 to 0.70452 and initial $^{143}\text{Nd}/^{144}\text{Nd}$ ratio ranges of 0.51257 to 0.51284 are primitive and very restricted in Late Cretaceous and younger intrusions, which are not metamorphosed in the Pebble district (Fig. 9). The Nd isotopic compositions ($\epsilon\text{Nd}_i = +4.6$ to $+6.3$) of any of the intrusions in the district, including those of the Talkeetna Arc, are not likely affected by external hydrothermal fluids because Nd is an immobile element, and thus a more robust tracer of radiogenic contamination. The Nd isotopic data from these intrusions overlap with those of the Talkeetna Arc volcanics in the West Talkeetna Mountains and along the Alaska Peninsula (Fig. 9; Rioux et al. 2007, 2010). In the Pebble district, the Sr and Nd isotopic compositions are similar for the Kaskanak granodiorite and the gabbro roof pendants interpreted as Jurassic in age (Fig. 9c). In contrast, older Triassic gabbros of the Tlikakila Complex located 100 km to the northwest (Wallace et al. 1989; Amato et al. 2007a) have quite variable Nd isotopic compositions ($\epsilon\text{Nd}_{215} = -1.2$ to $+9.3$), likely due to crustal contamination by an unknown radiogenic source, which are consistent with the observations of inherited Proterozoic and Archean zircons and the inferred metasomatic alteration by connate fluids noted above. Because inherited Proterozoic zircons are rare in Talkeetna Arc magmatic rocks (Pálfy et al. 1999; Amato et al. 2007c) and are absent from all of the Late Cretaceous to Eocene intrusions in the Pebble district, it is inferred that very little, if any, ancient continental crust exists beneath the Pebble district.

The primary contamination difference between the Jurassic and older basement rocks and the Late Cretaceous to Eocene igneous rocks is that the latter was contaminated by the Late Jurassic–Early Cretaceous Kahiltna flysch, the principal exposed country rock to the intrusions. Note that the Kahiltna flysch is more radiogenic than the Talkeetna Arc and the Tlikakila Complex, which are representative of the basement rocks from which the flysch is partially derived (Fig. 9). To constrain the amount of assimilation of the Kahiltna flysch required for Late Cretaceous and Paleocene intrusions, two-component mixing models (Faure 1998) were calculated between three selected igneous samples and an average composition of the Kahiltna flysch with isotopic compositions recalculated to both 90 and 65 m.y. ago to reflect the age of the mixing (Fig. 9; Appendix¹ E). Note that the Kahiltna flysch isotopic composition at 65 Ma would be slightly more radiogenic than at 90 or 125 Ma (Fig. 9a). The Sr isotopic data utilized for the Kahiltna flysch from Aleinikoff et al. (2000) ($^{87}\text{Sr}/^{86}\text{Sr}_{125 \text{ m.y.}} = 0.70549$ – 0.70715) overlaps with a single Sr isotopic analysis of the flysch locally at Pebble ($^{87}\text{Sr}/^{86}\text{Sr}_{125 \text{ m.y.}} = 0.70554$; Ayuso et al. 2013) and is therefore approximately representative. The three igneous end-members in the models include: (1) Kaskanak granodiorite, (2) a diorite sill, and (3) a Paleocene monzonite porphyry dike (see Appendix¹ E for trace element and isotopic compositions). The least radiogenic Late Cretaceous or Paleocene sample composition recorded in the district ($^{87}\text{Sr}/^{86}\text{Sr}_i = 0.70330$, $^{143}\text{Nd}/^{144}\text{Nd}_i = 0.512844$, $\epsilon\text{Nd}_i = +6.3$) is assumed to represent the minimum isotopic enrichment for homogenized parental melts supplied from the lower crust for the region and was utilized as the starting isotopic composition for the igneous rocks in the mixing models. The curvature of

the mixing models (Fig. 9b) reflects the whole-rock Sr and Nd composition of the igneous samples relative to the composition in the Kahiltna flysch (i.e., the susceptibility of the intrusions to be isotopically contaminated by the Kahiltna flysch). The ϵ_{Nd} vs. $1/\text{Nd}$ plot (Fig. 9c) suggests that maximum assimilation of the Kahiltna flysch by Late Cretaceous or Paleocene intrusions was predominantly minor (<20 wt%), except in the case of some narrow monzonite dikes or granodiorite sills that likely have assimilated up to 50 wt% locally. If a more radiogenic composition for the Kahiltna flysch is utilized (Fig. 9a), as might be the case for flysch stratigraphically high in the Kahiltna basin or closer to the suture zone with the Intermontane superterrane to the north, then the mixing-models would require a smaller percentage of assimilation of the flysch. Based on these models, the Kaskanak granodiorite is one of the least-radiogenic samples in the district (see Fig. 9c) and likely assimilated very little Kahiltna flysch (<10 wt%). Therefore, minor assimilation of the Kahiltna flysch likely had little effect on the fertility of Late Cretaceous melts.

Oxidation recorded by zircons

Among the REEs, only $\text{Ce}^{(3+,4+)}$ and $\text{Eu}^{(2+,3+)}$ occur in multiple valence states under natural magmatic conditions and thus may be used to monitor relative changes in the oxidation state of the melt. They are particularly useful in highly oxidized magmatic systems where other monitors (e.g., Fe-Ti oxides) are not applicable. Progressive oxidation during magmatic evolution and cooling has been documented in several porphyry environments (Ballard et al. 2002; Dilles et al. 2015). Chondrite-normalized Eu/Eu^* and Ce/Nd , a proxy for chondrite-normalized Ce/Ce^* , are used here to monitor the relative oxygen state of the melt upon late-stage zircon saturation (Olson 2015; Lu et al. 2016). Eu/Eu^* values ≥ 0.4 are typical of most porphyry Cu deposits and reflect oxidized and hydrous arc magmas (Ballard et al. 2002; Dilles et al. 2015). Ce/Nd (and Ce/Ce^*) ratios are also generally elevated and reflect oxidized conditions of mineralized porphyry intrusions, but overlap with data from barren intrusions and thus are not as effective as Eu/Eu^* for discriminating melt fertility. For example, Ce/Nd ratios of zircons from mineralized porphyries in the Chuquicamata district range from 0 to 77 compared to barren, older intrusions of the Montecristo Intrusive Complex, which have a range of 2 to 12 (Ballard et al. 2002). However, these mineralized porphyries contrast sharply with the range of zircon Ce/Nd ratios from mineralized intrusions in the neighboring Los Picos-Fortuna district of similar age. In the Los Picos-Fortuna district, mineralized porphyry intrusions have zircon Ce/Nd ratios ≤ 7 and pre-mineral barren intrusions completely overlap having ratios ranging from 2 to 10 (Ballard et al. 2002). Lu et al. (2016) also reported overlapping Ce/Nd ratios for zircon that range from 3 to 100 for intrusions genetically associated with porphyry $\text{Cu}\pm\text{Mo}\pm\text{Au}$ deposits and 0 to 40 from unrelated barren magmatic suites. We interpret the reported large range of Ce/Nd ratios in zircons from both barren and mineralized intrusions to reflect complications of varying oxidation states of melts in equilibrium with zircon and the presence of fractionating accessory minerals that sequester the REE^{3+} during late-stage differentiation and zircon crystallization (cf. Grimes et al. 2015). Titanite or apatite fractionation, for example, may modify the Ce anomaly by suppressing REE^{3+} from the melt.

In the Pebble district, nearly all mineralized intrusions of the Kaskanak batholith have zircon Eu/Eu^* ratios >0.4 (Fig. 10). Pre-mineral Cretaceous and post-mineral Paleocene intrusions in the district have similar zircon Eu/Eu^* values that suggests they also were hydrous and oxidized arc magmas. However, there is a clear distinction with regards to the diorite sills and the granodiorite of Koktuli Mountain that show consistently low- Eu/Eu^* values, indicating that they were likely both less-oxidized and less-hydrous relative to the mineralized intrusions. Zircon Ce/Nd ratios of mineralized intrusions range from 7 to 152 and mostly overlap with the pre-mineral Cretaceous intrusions that range from 4 to 126. Non-mineralized Paleocene intrusions have a smaller range of zircon Ce/Nd ratios that range from 7 to 53 and the Eocene Koktuli Mountain granodiorite in comparison is more restricted in range ($\text{Ce}/\text{Nd} = 10\text{--}22$).

Effects of titanite crystallization

Titanite, a common accessory mineral in relatively oxidized plutonic rocks, generally has a crystallization temperature of $<780^\circ\text{C}$ (Dilles 1987; Wones 1989; Piccoli et al. 2000; Mazdab and Wooden 2007; Mazdab et al. 2008) and occurs in many crystal-rich volcanic rocks (e.g., Fish Canyon Tuff; Bachmann and Bergantz 2008). In the Kaskanak batholith, titanite is the most abundant accessory mineral phase and the major sink for HFSEs and REEs. Magmatic titanite strongly incorporates all REEs, particularly the MREEs, with partition coefficients at low-magmatic temperatures of 700–800 °C that range between 100–1000 (Bachmann et al. 2005; Colombini et al. 2011). Unlike early crystallization or fractionation of amphibole or pyroxene, minor crystallization or fractionation of titanite can extremely depress the REE content of the melt and the relative proportions of each REE, and therefore readily effects geochemical proxies such as Sr/Y and La/Yb ratios (Bachmann et al. 2005; Richards and Kerrich 2007; Glazner et al. 2008; Colombini et al. 2011). During solidification of Kaskanak granodiorite, late-stage titanite fractionation reduces the HFSE and REE of remaining melt and together with other crystallizing minerals is responsible for differentiation to produce the most evolved and silicic granodiorite to granite porphyry dikes that are HFSE- and REE-poor (Figs. 6 and 8).

Crystal fractionation modeling of the Kaskanak batholith

Simple Rayleigh fractionation models are used here to assess lower-crustal and late-stage upper-crustal differentiation of the Kaskanak batholith. The most primitive Late Cretaceous rock compositions observed in the district include small volumes of shoshonite and porphyritic andesite dikes, the latter, which are spatially and temporally associated with the Kaskanak batholith (Olson 2015). These porphyritic andesite dikes represent a very small proportion (<1%) of the exposed Kaskanak batholith, suggesting most magmatic differentiation and maturation occurred in the deep or middle crust from which magma batches periodically rejuvenated the intermediate to felsic crystal mushes in the shallow crust.

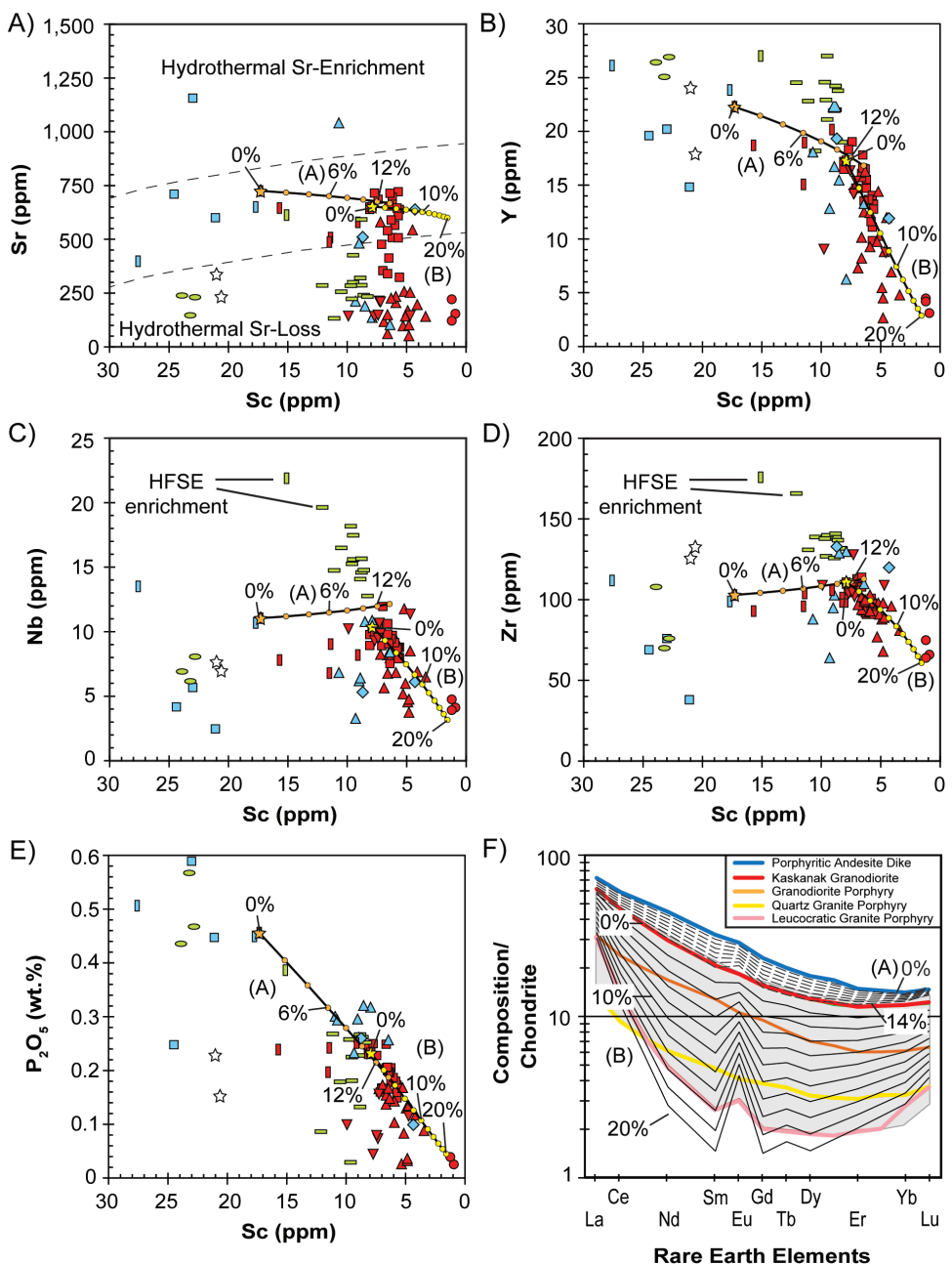
Model A: Differentiation of andesite parental melts.

Rayleigh fractionation modeling of a parental andesite composition to produce the Kaskanak granodiorite was undertaken for a series of trace elements (Model A; Table¹ 3) A best fit

$[\Sigma(R^2) = 5.5$, excluding Sr] was obtained by minimizing the residuals of most selected trace elements within 0–10% of the observed daughter melt composition (Table¹ 4). The model is largely constrained by observed mineral phases and Sc, Y, Nb, P_2O_5 , and REE, but the model fails to adequately describe Sr, which is readily affected by hydrothermal alteration (Fig. 14a). Model A also invokes up to 0.18 wt% allanite in the bulk cumulus that is required to reduce the LREE, whereas apatite, another LREE-bearing phase, is restricted by phosphorus (Fig. 14e). Allanite is rarely observed in these rocks (Olson 2015), possibly due to hydrothermal alteration to epidote. According to the model, ~10–14 wt% crystal fractionation of a hornblende-diorite bulk cumulus with 54.5 wt% amphibole, 32.5 wt%

plagioclase, 7.7 wt% magnetite, and 5.1 wt% apatite, and 0.18 wt% allanite could produce the observed range of granodiorite compositions (Fig. 14). Note that amphibole fractionation produces a minor depression of REE contents when the rhyolitic partition coefficients from Mount Mazama, Oregon, are applied (Bacon and Druitt 1998; Model A in Fig. 14f). The progressively greater depletions of Nb and REE are observed in the evolution sequence from the Kaskanak granodiorite to granite porphyry, which have an order of magnitude reduction in REE contents. Such depletions cannot be obtained by fractionation of any assemblage of high-temperature crystallizing minerals, such as Model A, and instead require fractionation of Nb- and REE-enriched titanite.

FIGURE 14. Rayleigh fractionation Models A and B for trace element evolution of the Kaskanak batholith using starting compositions, mineral-melt partition coefficients, and bulk compositions listed in Tables¹ 3 and 4. Black lines show fractionation paths in 2 wt% intervals for 1 to 14 wt% fractionation of a high-temperature assemblage for Model A (hornblende-plagioclase-magnetite-apatite-allanite) and 0 to 20 wt% fractionation of a lower-temperature assemblage for Model B (hornblende-plagioclase-magnetite-apatite-titanite-zircon). See text for details. (a) Sr vs. Sc, (b) Y vs. Sc, (c) Nb vs. Sc, (d) Zr vs. Sc, (e) P_2O_5 vs. Sc, and (f) chondrite-normalized REE spidergrams (McDonough and Sun 1995) for selected rock compositions and the observed range of granodiorite to granite compositions (gray field). Symbols of observed compositions as in Figure 4. Note that early fractionation of hornblende-rich assemblage A provides a good fit for early differentiation, but the titanite-bearing assemblage B is required to produce the large observed REE and HFSE depletions observed in the most silicic late porphyries



Estimating Nb and REE partition coefficients for titanite.

To model the effect of titanite-fractionation on melt, we necessarily constrained the partition coefficients for titanite in the Kaskanak granodiorite (Table¹ 3). In general, titanite partition coefficients (K_d) are poorly constrained for intermediate-felsic, metaluminous, low-temperature (e.g., 700–800 °C) calc-alkaline magmas, and published results for such compositions are highly variable and few in number (e.g., Bachmann et al. 2005; Colombini et al. 2011). We estimated titanite partition coefficients for the Kaskanak granodiorite from measured titanite_{max}/whole-rock_{max} concentrations utilizing only high-Y (>2000 ppm) titanite core analyses because the early high-Y titanite crystallized from a melt whose trace element content was initially most similar to whole-rock (Table¹ 3). These high-Y titanite cores are apparently unaffected by complicated late-stage magmatic processes (Fig. 12). We recognize that the whole-rock composition of the Kaskanak granodiorite from which titanite was analyzed is not likely representative of the melt in equilibrium with titanite during its growth, and thus our calculated partition coefficients are approximate. We infer that our titanite partition coefficients are relatively accurate for the REEs and HFSEs where the concentrations in titanite are much greater than the melt and are underestimated for compatible elements (e.g., Sr, Sc) that occur dominantly in other major mineral phases (e.g., plagioclase, amphibole, and magnetite).

Model B: Differentiation of the Kaskanak batholith. Rayleigh fractionation described in Model B addresses the second stage of low-temperature differentiation of the Kaskanak granodiorite to produce the observed compositional range of granodiorite and granite porphyries. The best fit for Model B [$\Sigma(R^2) = 2.9$] produces residuals within 0–10% of the observed daughter composition for most of the selected trace elements (Table¹ 4). The model estimates 16–20 wt% crystal fractionation of a bulk composition of 61.2 wt% amphibole, 28.0 wt% plagioclase, 2.7 wt% magnetite, 6.2 wt% apatite, 1.8 wt% titanite, and 0.07 wt% zircon (Fig. 14). The most differentiated granodiorite porphyry and quartz granite porphyry compositions shown in Figure 14f may also require additional apatite and allanite fractionation to suppress the LREE.

Eu and Ce anomalies revisited. A conclusion that results from the modeling is that fractionation of titanite, and to a lesser degree amphibole or apatite, can cause the Eu anomaly of the bulk rock to change from a small negative anomaly ($\text{Eu}/\text{Eu}^* < 1$) to a small positive anomaly ($\text{Eu}/\text{Eu}^* > 1$) because the fractionating assemblage incorporates REE³⁺ preferentially to Eu²⁺ (Fig. 14f). In general, positive Eu anomalies are not observed from whole-rock compositions, however; except for the modest positive anomalies in the most differentiated leucocratic granite porphyry dikes (Fig. 8d). Since a majority of the Eu in the melt occurs as Eu²⁺ over the range of natural oxygen fugacities of volcanic arc melts (e.g., Wilke and Behrens 1999), a likely explanation for this discrepancy between observed and modeled Eu contents is the oxidation of Eu²⁺ to Eu³⁺ in highly oxidized systems (Dilles et al. 2015) so that additional Eu³⁺ is incorporated by titanite. Note that the abundance of Eu or Ce in the melt is minuscule compared to the abundance of other oxidizing and reducing species and when the REE³⁺ are highly suppressed by titanite fractionation, a change in the Eu^{2+/3+} or Ce^{4+/3+} ratios would

not likely facilitate a change the oxidation state of the melt (i.e., the oxidation state of the melt is buffered). The likely result is that some of the remaining Eu²⁺ and Ce⁴⁺ is converted to a 3⁺ valence by equilibration with the melt. This affect would buffer the Eu anomaly of the melt near neutrality in oxidized systems, and could potentially decrease the Ce anomaly recorded in zircons (Fig. 10d) as titanite would diminish the partitioning of Ce³⁺ into zircon. Additional factors that could affect the oxidation state of the melt and the observed zircon Eu and Ce anomalies include the addition of new oxidizing or reducing species such as Fe^(2+,3+) or S^(2-,4+,6+) via assimilation of wall rocks or by the introduction of new melt by convection or recharge (Chambefort et al. 2008, 2013). Additionally, late-stage breakdown of magmatic anhydrite or sulfate bearing melt species to liberate SO₂ as a volatile species could increase the oxidation state of the melt (Dilles et al. 2015). Each of these scenarios are important to consider when critically evaluating the potential fertility of a given melt based on these redox-sensitive proxies.

Late Cretaceous petrogenesis and fertility

Late Cretaceous plutonic rocks in the Pebble district have a >300 km² areal extent and upper crustal volumes likely exceeding 1500 km³. They represent one of the best delineated Cretaceous igneous complexes identified in the SW Alaska Range. Major and trace element geochemistry, petrographic evidence, Ti-in-zircon estimates, and redox-sensitive proxies (e.g., zircon Eu anomalies, whole-rock V/Sc ratios) document evolution over a ~10 m.y. period from early, high-temperature, intermediate composition, moderately oxidized and hydrous melts to late low-temperature, silicic composition, and strongly oxidized and hydrous melts associated with ore formation. The earliest (~99–98 Ma) pre-mineral intrusions of diorite and monzodiorite contain minorly differentiated to intermediate SiO₂ contents, crystallized at relatively high temperatures (~930–730 °C Ti-in-zircon, Fig. 10), included both calc-alkaline and alkaline compositions, and were only modestly hydrous and oxidized (e.g., pyroxene-biotite-magnetite ± amphibole-bearing and likely ilmenite-poor or -free). The youngest and most evolved alkaline intrusions include monzonite porphyry dikes that contain magnetite and titanite assemblages reflecting more strongly oxidized conditions (Wones 1989). By the end of pre-mineral magmatism at ~95 Ma, parental melts had evolved to form the calc-alkaline hornblende-biotite granodiorite sills. The abundant amphibole in these sills indicates an evolution toward higher (≥4 wt%) water contents. Eu/Eu^{*} anomalies and large Ce/Nd ratios of zircons in the granodiorite sills indicate they were both highly oxidized and hydrous enough to suppress early plagioclase fractionation (Ballard et al. 2002; Dilles et al. 2015).

After an approximately 4 m.y. magmatic gap, the Kaskanak batholith was emplaced between 91–89 Ma. Early phases include equigranular granodiorite and several small porphyritic andesite dikes that were followed by a succession of more evolved porphyries, which were emplaced contemporaneously with ore formation (Lang et al. 2013; Olson 2015). The Kaskanak batholith makes up more than 60% of the footprint of Late Cretaceous plutonic rocks currently mapped in the Pebble district and has an inferred volume of ~900 km³. If the northern contact of the batholith were extended beneath cover 25 km further

to the northeast as proposed by Anderson et al. (2014) based on 3D inverse magnetic modeling, then the volume could be significantly larger (3–5×). Where the Kaskanak batholith is mapped, it is dominated by a mineral assemblage of hornblende, plagioclase, quartz, magnetite, and titanite. Together, this assemblage requires strongly hydrous and oxidized conditions that are notably consistent with the small Eu anomaly and large Ce anomaly of zircons. Zircon and titanite geothermometry indicate that these minerals crystallized at low temperatures of 680 to 800 °C similar to Ti-in-zircon temperatures estimates of other porphyry magmas (Dilles et al. 2015), and are consistent with differentiation of Kaskanak granodiorite to granite porphyry by the fractionating assemblage defined in Model B (Table¹ 3), which includes titanite. Ore-forming fluids are therefore closely associated with low-temperature and crystal-rich magma, and consistent with fluid saturation and separation from magma via cooling and crystallization (Burnham 1979).

The long lifespan and potentially the fertility of the Kaskanak batholith requires periodic injections of hot melts. Evidence for such injections are directly recorded in the trace element variations and Zr-in-titanite temperature increases in zones with low Y < 2000 (see Figs. 11 and 12). Hornblende rims are also commonly zoned (Fig. 11b) and have implications for the pressures (i.e., depth) of crystal growth and the rate of cooling upon final emplacement. Zoned hornblende is uncommon for plutonic igneous rocks where hornblende zonations may diffuse and homogenize when held at magmatic temperatures for extended periods of time (e.g., Houston and Dilles 2013). Instead, these zoned amphiboles also are supportive of periodic injections of melt into the shallow crust where the melt cooled relatively rapidly to preserve these textures.

The overall progressive evolution of Kaskanak batholith to more silicic compositions starts from early small volumes of andesite to a dominant volume of granodiorite to late small volumes of granite and subordinate andesite. This progression suggests that melt injections were primarily dacitic and progressively more differentiated with time. There is no clear evidence for Cretaceous basaltic magmas in the upper crustal environment exposed today, and subordinate porphyritic andesite dikes are the only intermediate magmas exposed that were emplaced contemporaneously with the Kaskanak batholith. Nonetheless, it is likely that primitive hydrous basalt or andesite melts contributed water, ore metals, and sulfur to the silicic melts of the Kaskanak batholith leading to the formation of one of the largest porphyry Cu-Au-Mo deposits in the world. We infer that the transfer of components from mafic to silicic melts via assimilation-fractional crystallization and recharge in a MASH or hot zone likely occurred in the deep crust. The low La/Yb and modest Sr/Y ratios suggest the MASH zone was in the base of thin crust (<30 km), and the high-temperature fractionating assemblage (Model A) had a composition equivalent to hornblende gabbro, which requires water-rich melts.

IMPLICATIONS

Protracted magmatic activity is a common feature of porphyry copper mineral belts where mineralized intrusions are commonly the culmination of long-lived magmatic activity (Seedorff et al. 2005; Chiaradia et al. 2009; Sillitoe 2010; Richards 2011).

In the Pebble district, magmatic activity spanned ~10 m.y. and culminated over the last 2 m.y. with the emplacement of the Kaskanak batholith (Lang et al. 2013; Olson 2015). Increased fertility associated with protracted magmatism in the Pebble district may be related to increased subduction components (e.g., water) supplied to the mantle wedge to promote partial melting. The initial hydrous, relatively oxidized, and potentially sulfate-rich (cf. Chambefort et al. 2008, 2013) basaltic melts likely included both alkaline and calc-alkaline compositions. They probably differentiated in the lower- to mid-crustal MASH or hot zones via fractionation and early removal of magnetite and amphibole and partial suppression of plagioclase to produce cooler highly oxidized, hydrous calc-alkaline andesite to dacite melts that ascended to the middle and upper crust.

Pebble, together with Grasberg, Bingham, and Kerr-Sulfurets-Mitchell, are among a handful of large porphyry deposits that have large endowments of copper, gold, and molybdenum. Seedorff et al. (2005) noted this porphyry metal association for both monzonitic Cu (Mo-Au) and tonalitic-granodioritic Cu-(Au-Mo) magma compositions and noted gold associated with syenitic and dioritic magma compositions. Gold-rich porphyry deposits are therefore broadly correlated with alkalic and intermediate composition magmas, which is the case at Pebble, Bingham, and Kerr-Sulfurets-Mitchell. Molybdenum, however, is well-known to be enriched in porphyry deposits that have more evolved melt compositions.

Why Pebble is both a gold-rich (~0.3 ppm) and a molybdenum-rich (~250 ppm) porphyry copper deposit is not completely resolved, but some inferences can be made. Many of the porphyry, epithermal, and intrusion-related deposits hosted in the volcanic arc crust of the Wrangellia composite terrane of southern Alaska are commonly gold-rich, so Pebble is not unique. We propose that chalcophile element enrichment of both copper and gold is an inherent part of the highly oxidized hydrous and sulfur-rich basalt magmas where oxidized conditions stabilize sulfate and minimize reduced sulfur, so that formation and fractionation of immiscible sulfide melt is inhibited (Carroll and Rutherford 1987, 1988; Keith et al. 1997; Tosdal et al. 2009; Chambefort et al. 2008, 2013; Dilles et al. 2015). Under more reduced conditions, copper- and gold-rich sulfide melt would form and potentially fractionate to reduce copper and gold contents of the magma and make it infertile (Botcharnikov et al. 2013; Li and Audétat 2013). Alternatively, interactions of hydrous and oxidized basalt in the MASH zone with Triassic and Jurassic mafic crystalline rocks and ultramafic cumulates may have been a possible source of sulfide and trace metal enrichment. In the Kennecott district in southeast Alaska (Fig. 1), for example, some of the world's highest grade copper-(silver) ores ever mined are thought to be scavenged from the Triassic Nikolai Greenstone host-rocks in the Wrangellia terrane (MacKevett et al. 1997). In south-central Alaska, gabbroic rocks of the Jurassic Talkeetna Arc are also locally enriched in base metals such as Cr, Ni, and Cu (DeBari and Sleep 1991; Greene et al. 2006), and in the Pebble district, gabbro roof pendants contain magmatic sulfide and bulk-compositions containing up to 50 ppm Ni and 350 ppm Cu. An identifiable crustal source for gold is elusive. Gold content is near crustal abundance and is not anomalous in the Nikolai Greenstone of the Wrangellia terrane nor in the Jurassic gabbro and basalt roof pendants and Late Cretaceous biotite

pyroxenite cumulates in the Pebble district where the rocks are unaffected by significant hydrothermal alteration.

The primitive Sr and Nd isotopic compositions of Pebble magmas preclude the presence of old and silicic Mo-enriched continental crust underlying much of the SW Alaska Range, except for perhaps near the suture zone. Rather, molybdenum must ultimately be derived from partial melting of the mantle wedge or from assimilation of older Mesozoic mafic to intermediate arc crust of the Peninsula terrane. Neither source is typical of porphyry deposits with abundant molybdenum. The Cretaceous pre-mineral alkalic magmas at Pebble may have provided Mo-enrichment to the crust because alkalic magmas are commonly enriched in Mo (Carten et al. 1993; Seedorff et al. 2005). Nonetheless, both the long-time scale of igneous processes, and the strong differentiation from inferred hydrous basalt to andesite and mineralizing granodiorite to granite melts would have enriched Mo in end-stage granite porphyry intrusions because of the incompatible behavior of Mo in melts (Candela and Holland 1986). The requirement of multiple events of hot silicic melt recharge followed by cooling and crystallization would have additionally enriched Mo in the latest melts.

The Pebble deposit therefore appears to have formed via relatively typical arc-magmatic processes developed in relatively thin and primitive mafic to intermediate crust. It is related to strongly oxidized hydrous magmatism that extended over a period of 10 m.y. Episodic magma recharge, and assimilation and fractional crystallization are implicated in production of late-stage granodiorite to granite melt compositions with inferred elevated water, sulfur, chlorine, Cu, Au, and Mo contents. Cooling and crystallization led to further magmatic differentiation and emplacement of multiple generations of porphyry dikes with each episode accompanied by magmatic-derived ore fluids. These implications are largely inferred from whole-rock trace element and isotope geochemistry, mineral geochemistry, and crystal fractionation modeling constrained by petrographic observations.

ACKNOWLEDGMENTS

The authors thank the many geologists employed by the Pebble Partnership who facilitated core sampling and logging, and provided necessary logistical support for the project. We thank Matt Coble and Joe Wooden of the USGS-Stanford SHRIMP-RG lab for assistance with data processing and interpretation. We greatly thank Eric Seedorff and an anonymous reviewer for their feedback, which greatly improved this manuscript. Additionally, we thank fellow OSU VIPER faculty and students for thoughtful discussions and support. This research was supported by the Pebble Partnership, and in part by NSF Grants EAR-1049792 and EAR-1447730.

REFERENCES CITED

- Aleinikoff, J.N., Plafker, G., and Nokleberg, W.J. (1988) Middle Pennsylvanian plutonic rocks along the southern margin of Wrangellia. In T.D. Hamilton and J.P. Galloway, Eds., *The United States Geological Survey in Alaska: Accomplishments during 1987*. U.S. Geological Survey, Circular, 1016, 110–113.
- Aleinikoff, J.N., Farmer, G.L., Rye, R.O., and Nokleberg, W.J. (2000) Isotopic evidence for the sources of Cretaceous and Tertiary granitic rocks, east-central Alaska: Implications for the tectonic evolution of the Yukon-Tanana Terrane. *Canadian Journal of Earth Sciences*, 37, 945–956.
- Amato, J.M., Bogar, M.J., Gehrels, G.E., Farmer, G.L., and McIntosh, W.C. (2007a) The Tlikakila Complex in southern Alaska: A supra-subduction-zone ophiolite between the Wrangellia Composite terrane and North America. *The Geological Society of America Special Papers*, 431, 227–252.
- Amato, J.M., Foley, C., Heizler, M., and Esser, R. (2007b) $^{40}\text{Ar}/^{39}\text{Ar}$ and U-Pb geochronology, geochemistry, and tectonic setting of three episodes of Cretaceous-Eocene calc-alkaline magmatism in the Lake Clark region, southwestern Alaska. *Geological Society of America Special Papers*, 431, 455–475.
- Amato, J.M., Rioux, M.E., Kelemen, P.B., Gehrels, G.E., Clift, P.D., Pavlis, T.L., and Draut, A.E. (2007c) U-Pb geochronology of volcanic rocks from the Jurassic Talkeetna Formation and detrital zircons from prearc and postarc sequences: Implications for the age of magmatism and inheritance in the Talkeetna arc. *The Geological Society of America Special Papers*, 431, 253–271.
- Anderson, E.D., Zhou, W., Li, Y., Hitzman, M.W., Monecke, T., Lang, J.R., and Kelley, K.D. (2014) Three-dimensional distribution of igneous rocks near the Pebble porphyry Cu-Au-Mo deposit in southwestern Alaska: Constraints from regional-scale aeromagnetic data. *Geophysics*, 79, B63–B79.
- Annen, C., Blundy, J.D., and Sparks, R.S.J. (2006) The genesis of intermediate and silicic magmas in deep crustal hot zones. *Journal of Petrology*, 47, 505–539.
- Ayuso, R.A., Kelley, K.D., Eppinger, R.G., and Forni, F. (2013) Pb-Sr-Nd isotopes in surficial materials at the Pebble Porphyry Cu-Au-Mo deposit, southwestern Alaska: Can the mineralizing fingerprint be detected through cover? *Economic Geology*, 108, 543–562.
- Bachmann, O., and Bergantz, G.W. (2008) Rhyolites and their source mushes across tectonic settings. *Journal of Petrology*, 49, 2277–2285.
- Bachmann, O., Dungan, M.A., and Bussy, F. (2005) Insights into shallow magmatic processes in large silicic magma bodies: The trace element record in the Fish Canyon magma body, Colorado. *Contributions in Mineralogy and Petrology*, 149, 338–349.
- Bacon, C.R., and Druitt, T.H. (1998) Compositional evolution of the zoned calcalkaline magma chamber of Mount-Mazama, Crater Lake, Oregon. *Contributions to Mineralogy and Petrology*, 98, 224–256.
- Bacon, C.R., Vazquez, J.A., and Wooden, J.L. (2012) Peninsular terrane basement ages recorded by Paleozoic and Paleoproterozoic zircon in gabbro xenoliths and andesite from Redoubt Volcano, Alaska. *Geological Society of America Bulletin*, 224, 24–34.
- Ballard, J.R., Palin, J.M., and Campbell, I.H. (2002) Relative oxidation states of magmas inferred from Ce(IV)/Ce(III) in zircon: Application to porphyry copper deposits of northern Chile. *Contributions to Mineralogy and Petrology*, 144, 347–364.
- Barker, F. (1987) Cretaceous Chisana island arc of Wrangellia, eastern Alaska. *Geological Society of America Abstracts with Programs*, 19, 580.
- Barnes, D.F. (1977) Bouguer gravity map of Alaska. U.S. Geological Survey Map, GP-913, 1:250,000. Available: <http://pubs.er.usgs.gov/publication/gp913/>.
- Beard, J.S., and Barker, F. (1989) Petrology and tectonic significance of gabbros, tonalities, shoshonites, and anorthosites in a late Paleozoic arc-root complex in the Wrangellia terrane, southern Alaska. *Journal of Geology*, 97, 667–683.
- Black, L.P., Kamo, S.L., Allen, C.M., Aleinikoff, J.N., Davis, D.W., Korsch, R.J., and Foudoulis, C. (2003) TEMORA 1: A new zircon standard for Phanerozoic U-Pb geochronology. *Chemical Geology*, 200, 155–170.
- Botcharnikov, R.E., Holtz, F., Mungall, J.E., Beermann, O., Linnen, R.L., and Garbe-Schönberg, D. (2013) Behavior of gold in a magma at sulfide-sulfate transition: Revisited. *American Mineralogist*, 98, 1459–1464.
- Bouley, B.A., St. George, P., and Wetherbee, P.K. (1995) Geology and discovery at Pebble Copper, a copper-gold porphyry system in southwest Alaska. In T.G. Schroeder, Ed., *Porphyry Deposits of the Canadian Cordillera of North America*. Canadian Institute of Mining, Metallurgy, and Petroleum Special Volume, 46, 422–435.
- Brooks, C.K., Henderson, P., and Rønbo, J.G. (1981) Rare-earth partition between allanite and glass in the obsidian of Sandy Braes, Northern Ireland. *Mineralogical Magazine*, 44, 157–160.
- Burnham, C.W. (1979) Magmas and hydrothermal fluids. In H.L. Barnes, Ed., *Geochemistry of Hydrothermal Ore Deposits*, 2nd ed., p. 71–136. Wiley, New York.
- Burnham, C.W., and Ohmoto, H. (1980) Late stage process of felsic magmatism. In S. Ishihara and S. Takenouchi, Eds., *Granitic Magmatism and Related Mineralization*. Society of Mining Geologists of Japan, 8, 1–11.
- Candela, P.A. (1992) Controls on ore metal ratios in granite-related ore systems: An experimental and computational approach. *Transactions of the Royal Society of Edinburgh: Earth Sciences*, 83, 317–326.
- Candela, P.A., and Holland, H.D. (1986) A mass transfer model for copper and molybdenum in magmatic hydrothermal system: The origin of porphyry-type ore deposits. *Economic Geology*, 81, 1–19.
- Candela, P.A., and Piccoli, P.M. (2005) Magmatic processes in the development of porphyry type ore systems. *Economic Geology*, 100th Anniversary Volume, 25–37.
- Carroll, M.R., and Rutherford, M.J. (1987) The stability of igneous anhydrite: Experimental results and implications for sulfur behavior in the 1982 El Chichón trachyanandesite and other evolved magmas. *Journal of Petrology*, 28, 781–801.
- (1988) Sulfur speciation in hydrous experimental glasses of varying oxidation state: Results from measured wavelength shifts of sulfur X-rays. *American Mineralogist*, 73, 845–849.
- Carten, R.B., White, W.H., and Stein, H.J. (1993) High-grade granite-related molybdenum systems: Classification and origin. In R.V. Kirkham, W.D. Sinclair, R.I. Thorpe, and J.M. Duke, Eds., *Mineral Deposit Modeling*. Geological Association of Canada Special Paper, 40, 521–554.
- Chambefort, I., Dilles, J.H., and Kent, J.R. (2008) Anhydrite-bearing andesite and dacite as a source for sulfur in magmatic-hydrothermal mineral deposits. *Geology*, 36, 719–722.
- Chambefort, I., Dilles, J.H., and Longo, A.A. (2013) Amphibole geochemistry of the Yanacocha Volcanics, Peru: Evidence for diverse sources of magmatic volatiles related to gold ores. *Journal of Petrology*, 54, 1017–1046.
- Chiaradia, M., Merino, D., and Spikings, R. (2009) Rapid transition to long-lived deep crustal magmatic maturation and the formation of giant porphyry-related mineralization (Yanacocha, Peru). *Earth and Planetary Science Letters*, 288, 505–515.
- Claiborne, L.L., Miller, C.F., and Wooden, J.L. (2010) Trace element composition

- of igneous zircon: A thermal and compositional record of the accumulation and evolution of a large silicic batholith, Spirit Mountain, Nevada. *Contributions to Mineralogy and Petrology*, 160, 511–531.
- Clift, P., Draut, A., Kelemen, P.B., Blusztajn, J., and Greene, A.R. (2005) Stratigraphic and geochemical evolution of an oceanic arc upper crustal section: The Jurassic Talkeetna Volcanic Formation, south-central Alaska. *Geological Society of America Bulletin*, 117, 902–925.
- Cline, J.S., and Bodnar, R.J. (1991) Can economic porphyry copper mineralization be generated by a typical calc-alkaline melt? *Journal of Geophysical Research*, 96, 8113–8126.
- Colombini, L.L., Miller, C.F., Gualda, G.A.R., Wooden, J.L., and Miller, J.S. (2011) Sphene and zircon in the Highland Range, volcanic sequence (Miocene, southern Nevada, U.S.A.): Elemental partitioning, phase relations, and influence on evolution of silicic magma. *Mineralogy and Petrology*, 102, 29–50.
- Coney, P.J., and Jones, D.L. (1985) Accretion tectonics and crustal structure in Alaska. *Tectonophysics*, 119, 265–283.
- Csejtey, B. Jr., Nelson, W.H., Jones, D.L., Silberling, N.J., Dean, R.M., Morris, M.S., Lanphere, M.A., Smith, J.G., and Silberman, M.L. (1978) Reconnaissance geologic map and geochronology, Talkeetna Mountains quadrangle, northern part of Anchorage quadrangle, and southwest corner of Healy quadrangle, Alaska. U.S. Geological Survey Open-File Report 788-558-A, 60 p., scale 1:250,000.
- Csejtey, B. Jr., Cox, D.P., Evarts, R.C., Stricker, G.D., and Foster, H.L. (1982) The Cenozoic Denali fault system and the Cretaceous accretionary development of southern Alaska. *Journal of Geophysical Research*, 87, 3741–3754.
- DeBari, S.M., and Sleep, N.H. (1991) High-Mg, low-Al bulk composition of the Talkeetna Arc, Alaska: Implications for primary magmas and the nature of arc crust. *Geological Society of America Bulletin*, 103, 37–47.
- Detterman, R.L., and Reed, B.L. (1980) Stratigraphy, structure, and economic geology of the Iliamna Quadrangle, Alaska. U.S. Geological Survey Bulletin, 1368-B, 86 p.
- Detterman, R.L., Case, J.E., Miller, J.W., Wilson, F.H., and Yount, M.E. (1996) Stratigraphic framework of the Alaska Peninsula. U.S. Geological Survey Bulletin 1969-A, 74 p., <http://pubs.usgs.gov/pubs/id/3754>.
- Dilles, J.H. (1987) The petrology of the Yerington batholith, Nevada: Evidence for the evolution of porphyry copper ore fluids. *Economic Geology*, 82, 1750–1789.
- Dilles, J.H., Kent, A.J.R., Wooden, J.L., Tosdal, R.M., Koleszar, A., Lee, R.G., and Farmer, L.P. (2015) Zircon compositional evidence for sulfur-degassing from ore-forming arc magmas. *Economic Geology*, 110, 241–251.
- Ewart, A., and Griffin, W.L. (1994) Application of proton-microprobe data to trace-element partitioning in volcanic-rocks. *Chemical Geology*, 117, 251–284.
- Faure, G. (1998) Principles and Applications of Geochemistry, 2nd ed., p. 335–338. Prentice Hall, New Jersey.
- Ferry, J.M., and Watson, E.B. (2007) New thermodynamic models and revised calibrations for the Ti-in-zircon and Zr-in-rutile thermometers. *Contributions to Mineralogy and Petrology*, 154, 429–437.
- Fujimaki, H. (1986) Partition-coefficients of Hf, Zr, and REE between zircon, apatite, and liquid. *Contributions to Mineralogy and Petrology*, 94, 42–45.
- Gardener, M.C., Bergman, S.C., MacKevett, E.M. Jr., Plafker, G., Cambell, R.C., Cushing, G.W., Dodds, C.J., and McClelland, W.D. (1988) Middle Pennsylvanian pluton stitching of Wrangellia and the Alexander Terrane, Wrangell Mountains, Alaska. *Geology*, 15, 967–971.
- Gaunt, J.D., Rebaliati, C.M., Lang, J.R., Titley, E., Melis, L., Barratt, D., and Hodgson, S. (2010) Technical report on the 2009 program and update on mineral resources and metallurgy, Pebble copper-gold-molybdenum project, Alaska, 195 p., <http://www.sedar.com/>.
- Glazner, A., Coleman, D., and Bartley, J. (2008) The tenuous connection between high-silica rhyolites and granodiorite plutons. *Geology*, 36, 183–186.
- Goldfarb, R.J., Ayuso, R., Miller, M.L., Ebert, S.W., Marsh, E.E., Petsel, S.A., Miller, L.D., Bradley, D., Johnson, C., and McClelland, W. (2004) The Late Cretaceous Donlin Creek Gold Deposit, Southwest Alaska: Controls on epizonal ore formation. *Economic Geology*, 99, 643–671.
- Goldfarb, R.J., Anderson, E., and Hart, C.J.R. (2013) Tectonic setting of the Pebble and other copper-gold-molybdenum porphyry deposits within the evolving middle Cretaceous continental margin of northwestern North America. *Economic Geology*, 108, 405–419.
- Gregory, M.J. (2017) A fluid inclusion and stable isotope study of the Pebby porphyry copper-gold-molybdenum deposit, Alaska. *Ore Geology Reviews*, 80, 1279–1303.
- Gregory, M.J., Lang, J.R., Gilbert, S., and Hoal, K.O. (2013) Geometallurgy of the Pebble Porphyry Copper-Gold-Molybdenum Deposit, Alaska: Implications for gold distribution and paragenesis. *Economic Geology*, 108, 463–482.
- Greene, A.R., DeBari, S.M., Kelemen, P.B., Blusztajn, J., and Clift, P.D. (2006) A detailed geochemical study of island arc crust: The Talkeetna Arc section, south-central Alaska. *Journal of Petrology*, 47, 1051–1093.
- Grimes, C.B., Wooden, J.L., Cheadle, M.J., and John, B.E. (2015) “Fingerprinting” tectono-magmatic provenances using trace elements in igneous zircon. *Contributions to Mineralogy and Petrology*, 170, 5–6, 1–26.
- Hampton, B.A., Ridgway, K.D., and Gehrels, G.E. (2010) A detrital record of Mesozoic island arc accretion and exhumation in the North American Cordillera: U-Pb geochronology of the Kahiltna Basin, southern Alaska. *Tectonics*, 29, TC4015.
- Harraden, C.L., McNulty, B.A., Gregory, M.J., and Lang, J.R. (2013) Shortwave infrared spectral analysis of hydrothermal alteration associated with the Pebble porphyry copper-gold-molybdenum deposit, Iliamna, Alaska. *Economic Geology*, 108, 483–494.
- Hart, C.J., Goldfarb, R.J., Lewis, L.L., and Mair, J.L. (2004) The Northern Cordilleran Mid-Cretaceous plutonic province: Ilmenite/magnetite-series granitoids and intrusion-related mineralisation. *Resource Geology*, 54, 253–280.
- Hart, C.J., Lang, J.R., Goldfarb, R.J., and Farmer, G.L. (2010) Intrusive rocks associated with the Pebble porphyry Cu-Au-Mo deposit, southwest Alaska. *Geological Society of America, Abstract 290-8, Denver Annual Meeting*, <https://gsa.confex.com/gsa/2010AM/webprogram/Paper182738.html>.
- Hayden, L.A., Watson, E.B., and Wark, D.A. (2008) A thermobarometer for sphene (titaniite). *Contributions to Mineralogy and Petrology*, 155, 529–540.
- Hildreth, W., and Moorbath, S. (1988) Crustal contributions to arc magmatism in the Andes of central Chile. *Contributions to Mineralogy and Petrology*, 98, 455–489.
- Hoskin, P.W., and Schaltegger, U. (2003) The composition of zircon and igneous and metamorphic petrogenesis. *Reviews in Mineralogy and Geochemistry*, 53, 27–62.
- Houston, R.A., and Dilles, J.H. (2013) Structural geologic evolution of the Butte District, Montana. *Economic Geology*, 108, 1397–1424.
- Hults, C.P., Wilson, F.H., Doneck, R.A., and O’Sullivan, P.B. (2013) Two flysch belts having distinctly different provenance suggest no stratigraphic link between Wrangellia composite terrane and the paleo-Alaskan margin. *Lithosphere*, 5, 575–594.
- Iriondo, A., Kunk, M.J., and Wilson, F.H. (2003) $^{40}\text{Ar}/^{39}\text{Ar}$ geochronology of igneous rocks in the Taylor Mountains and Dillingham Quadrangles in SW Alaska. U.S. Geological Survey Open-File Report, 03-0421, 32 p., <http://pubs.usgs.gov/of/2003/ofr-03-421>.
- Irvine, T., and Baragar, W. (1971) A guide to the chemical classification of the common volcanic rocks. *Canadian Journal of Earth Sciences*, 8, 523–548.
- Ishikawa, Y., Sawaguchi, T., Iwaya, S., and Horiochi, M. (1976) Delineation of prospecting targets for Kuroko deposits based on modes of volcanism of underlying dacite and alteration halos. *Mining Geology*, 26, 105–117.
- Johnson, D.M., Hooper, P.R., and Conrey, R.M. (1999) XRF analysis of rocks and minerals for major and trace elements on a single low dilution Li-tetraborate fused bead. *Advances in X-ray Analysis*, 41, 843–867.
- Jones, D.L., Silberling, N.J., Gilbert, W., and Coney, P. (1982) Character, distribution, and tectonic significance of accretionary terranes in the central Alaska Range. *Journal of Geophysical Research*, 87, 3709–3717.
- Jones, D.L., Silberling, N.J., and Coney, P.J. (1986) Collision tectonics in the Cordillera of western North America: Examples from Alaska. In M.P. Coward and A.C. Ries, Eds., *Collision Tectonics*. Geological Society of London, Special Publication, 19, 367–389.
- Kalbas, J.L., Ridgeway, K.D., and Gehrels, G.E. (2007) Stratigraphy, depositional systems, and provenance of the Lower Cretaceous Kahiltna assemblage, Western Alaska Range: Basin development in response to oblique collision. *Geological Society of America Special Paper*, 431, 307–344.
- Kay, S.M., and Mpodozis, C. (2001) Central Andean ore deposits linked to evolving shallow subduction systems and thickening crust. *GSA Today*, 11, 4–9.
- Keith, J.D., Whitney, J.A., Hattori, K., Ballantyne, G.H., Christiansen, E.H., Barr, D.L., Cannan, T.N., and Hook, C.J. (1997) The role of magmatic sulfides and mafic alkaline magmas in the Bingham and Tintic Mining Districts, Utah. *Journal of Petrology*, 38, 1679–1690.
- Klein, M., Stosch, H.G., and Seck, H.A. (1997) Partitioning of high field strength elements between amphibole and quartz-dioritic to tonalitic melts: An experimental study. *Chemical Geology*, 138, 257–271.
- Knaack, C., Cornelius, S., and Hooper, P. (1994) Trace element analyses of rocks and minerals by ICP-MS (Online). Peter Hooper GeoAnalytical Lab, Washington State University, http://environment.wsu.edu/facilities/geolab/technotes/icp-ms_method.html (accessed May 15, 2012).
- Lang, J.R., Gregory, M.J., Rebaliati, C.M., Payne, J.G., Oliver, J.L., and Roberts, K. (2013) Geology and magmatic-hydrothermal evolution of the giant Pebble porphyry copper-gold-molybdenum deposit, southwest Alaska. *Economic Geology*, 108, 437–462.
- Large, R.R., Gemmell, J.B., Paulick, H., and Huston, D.L. (2001) The alteration box plot: A simple approach to understanding the relationship between alteration, mineralogy, and lithogeochemistry associated with volcanic-hosted massive sulfide deposits. *Economic Geology*, 96, 957–971.
- Le Maître, R.W.B., Dudek, P., Keller, A., Lameyre, J., Le Bas, J., Sabine, M.J., Schmid, P.A., Sorensen, R., Streckeisen, H., Woolley, A., and Zanettin, A.R. (1989) A classification of igneous rocks and glossary of terms: Recommendations of the International Union of Geological Sciences, Subcommission on the Systematics of Igneous Rocks. International Union of Geological Sciences, No. 552.3 CLA, 193 p.
- Li, Y., and Audébat, A. (2013) Gold solubility and partitioning between sulfide liquid, monosulfide solid solution and hydrous mantle melts: Implications for the formation of Au-rich magmas and crust–mantle differentiation. *Geochimica et Cosmochimica Acta*, 118, 247–262.
- Loewen, M.W., and Kent, A.J.R. (2012) Sources of elemental fractionation and uncertainty during the analysis of semi-volatile metals in silicate glasses using LA-ICP-MS. *Journal of Analytical and Atomic Spectrometry*, 27, 1502–1508.
- Loucks, R.R. (2014) Distinctive composition of copper-ore-forming arc magmas. *Australian Journal of Earth Sciences*, 61, 5–16.

- Lu, Y.J., Loucks, R.R., Fiorentini, M.L., McCuaig, T.C., Evans, N.J., Yang, Z.M., Hou, Z.Q., Kirkland, C.L., Parra-Avila, L.A., and Kobussen, A. (2016) Zircon compositions as a pathfinder for porphyry Cu ± Mo ± Au deposits. *Society of Economic Geologists Special Publication*, 19, 329–347.
- MacKevett, E.M. Jr., Cox, D.P., Potter, R.W., and Silberman, M.L. (1997) Kennecott-type deposits in the Wrangell Mountains, Alaska high-grade copper ores near a basalt-limestone contact. *Economic Geology*, Monograph, 9, 66–89.
- Mahood, G.A., and Hildreth, E.W. (1983) Large partition coefficients for trace elements in high-silica rhyolites. *Geochimica et Cosmochimica Acta*, 47, 11–30.
- Mattinson, J.M. (2005) U-Pb inter-laboratory calibrations using zircon samples: Application of the new CA-TIMS technique. *Goldschmidt Conference Abstracts, High-Precision Geochronology*, A319.
- Mazdab, F.K., and Wooden, J.L. (2006) Trace element analysis in zircon by ion microprobe (SHRIMP-RG): Technique and applications. *Geochimica et Cosmochimica Acta*, 70, A405.
- (2007) Trace element variability in titanite from diverse geologic environments. *Geological Society of America, Abstracts with Programs*, 39, 406.
- Mazdab, F.K., Johnson, D.A., and Barton, M.D. (2008) Trace element characterization of hydrothermal titanite from ion-oxide Cu-Au (IOCG) mineralization. *Geochimica et Cosmochimica Acta*, 72, A609.
- McDonough, W.F., and Sun, S.S. (1995) The composition of the Earth. *Chemical Geology*, 120, 223–253.
- Miková, J., and Denková, P. (2007) Modified chromatographic separation scheme for Sr and Nd isotope analysis in geological silicate samples. *Journal of Geosciences*, 52, 221–226.
- Naney, M.T. (1983) Phase equilibria of rock forming ferromagnesian silicates in granitic systems. *American Journal of Sciences*, 283, 993–1033.
- Nokleberg, W.J., Plafker, G., and Wilson, F.H. (1994) Geology of south-central Alaska. In G. Plafker and H.C. Berg, Eds, *The geology of Alaska*. Geological Society of America, Boulder, Colorado, G-1, 311–366.
- Olson, N.H. (2015) The Geology, Geochronology, and Geochemistry of the Kaskanak Batholith, and other Late Cretaceous to Eocene magmatism at the Pebble Porphyry Cu-Au-Mo deposit, SW Alaska, 248 p. M.S. thesis, Oregon State University, Corvallis, Oregon.
- Pálfy, J., Smith, P.L., Mortensen, J.K., and Friedman, R.M. (1999) Integrated ammonite biochronology and U-Pb geochronometry from a basal Jurassic section in Alaska. *Geological Society of America Bulletin*, 111, 1537–1549.
- Piccoli, P., Candela, P.A., and Ribera, M. (2000) Interpreting magmatic processes from accessory phases: titanite—A small-scale recorder of large-scale processes. In B. Barbarin, W.E. Stephens, B. Bonin, J.L. Bouchéz, D.B. Clarke, M. Cuney, and H. Martin, Eds., 4th Hutton Symposium. *Transactions of the Royal Society of Edinburgh, Earth Science*, 91, 27–267.
- Plafker, G., Nokleberg, W.J., and Lull, J.S. (1989) Bedrock geology and tectonic evolution of the Wrangellia, Peninsular, and Chugach terranes along the Trans-Alaskan Crustal Transect in the northern Chugach Mountains and southern Copper River basin, Alaska. *Journal of Geophysical Research*, 94, 4255–4295.
- Rebagliati, M., and Lang, J.R. (2015) Discovery of the Pebble porphyry Cu-Au-Mo deposit, Southwest Alaska: History and exploration methods. In D. Wood, Ed., *Trifecta Talks on Discovery, Exploration, and Geometallurgy*. Society of Economic Geology, Annual meeting, Halifax, Australia.
- Reed, B.L., and Lanphere, M.A. (1972) Generalized geologic map of the Alaska-Aleutian Range batholith showing potassium-argon ages of the plutonic rocks. U.S. Geological Survey Misc. Field Studies Map, MF-372, <http://pubs.er.usgs.gov/publication/mf372/>.
- Reiners, P.W., Nelson, B.K., and Nelson, S.W. (1996) Evidence of multiple mechanism of crustal contamination of magma from compositionally zoned plutons and associated ultramafic intrusions of the Alaska Range. *Journal of Petrology*, 37, 261–292.
- Ricardo, M.S.L. (2009) A comparison of deposit and regional intrusives, Pebble, Alaska, 74 p. B.S. thesis, University of Alberta, Calgary, Canada.
- Richards, J.P. (1995) Alkaline-type epithermal gold deposits—A review. In J.F.H. Thompson, Ed., *Magmas, Fluids, and Ore Deposits*. Mineralogical Association of Canada Short Course Series, 23, 367–400, <http://www.empr.gov.bc.ca/Mining/Geoscience/PublicationsCatalogue/OpenFiles/1998/Documents/OF1998-08/h3-43.pdf>.
- (2011) High Sr/Y arc magmas and porphyry Cu ± Mo ± Au deposits: Just add water. *Economic Geology*, 106, 1075–1081.
- Richards, J.P., and Kerrich, R. (2007) Special paper: Adakite-like rocks: Their diverse origins and questionable role in metallogenesis. *Economic Geology*, 102, 537–576.
- Richards, J.P., Spell, T., Rameh, E., Razique, A., and Fletcher, T. (2012) High Sr/Y magmas reflect arc maturity, high magmatic water content, and porphyry Cu ± Mo ± Au potential: Examples from the Tethyan arcs of central and eastern Iran and western Pakistan. *Economic Geology*, 107, 295–332.
- Rioux, M., Hacker, B., Mattinson, J., Kelemen, P., Blusztajn, J., and Gehrels, G. (2007) Magmatic development of an intra-oceanic arc: High precision U-Pb zircon and whole rock isotopic analyses from the accreted Talkeetna Arc, south-central Alaska. *Geological Society of America Bulletin*, 119, 1168–1184.
- Rioux, M., Mattinson, J., Hacker, B., Kelemen, P., Blusztajn, J., Hanghøj, K., and Gehrels, G. (2010) Intermediate to felsic middle crust in the accreted Talkeetna Arc, the Alaska Peninsula and Kodiak Island, Alaska: An analogue for low-velocity middle crust in modern arcs. *Tectonics*, 29, TC3001.
- Ryerson, F.J., and Watson, E.B. (1987) Rutile saturation in magmas: Implications for Ti-Nb-Ta depletion in island-arc basalts. *Earth and Planetary Science Letters*, 86, 225–239.
- Schrader, C.M. (2001) Geochronology and geology of the Pebble Cu-Au-Mo porphyry and the Sill Au-Ag epithermal deposits, southwest Alaska, 109 p. M.S. thesis, University of Georgia, Athens.
- Seedorff, E., Dilles, J.H., Proffett, J.M. Jr., Einaudi, M.T., Zurich, L., Stavast, W.J.A., Johnson, D.A., and Barton, M.D. (2005) Porphyry deposits: Characteristics and origin of hypogene features. *Economic Geology*, 100th Anniversary Volume, 251–298.
- Sillitoe, R.H. (2010) Porphyry copper systems. *Economic Geology*, 105, 3–41.
- Silberling, N.J., Jones, D.L., Monger, J.W.H., Coney, P.H., Berg, H.C., and Plafker, G. (1994) Lithotectonic terrane map of Alaska and adjacent parts of Canada. In G. Plafker, and H.C. Berg, Eds., *The geology of Alaska*. Geological Society of America, *The geology of North America*, G-1, plate 3, 1 sheet, 1:7, 500,000.
- Snyder, D.C., and Hart, W.K. (2007) The White Mountain Granitoid Suite: Isotopic constraints on source reservoirs for Cretaceous magmatism within the Wrangellia Terrane. *Geological Society of America Special Paper*, 431, 379–399.
- Sun, S.S., and McDonough, W.F. (1989) Chemical and isotopic systematics of oceanic basalts: Implications for mantle composition and process. *Geological Society of London Special Publication*, 42, 313–345.
- Tanaka, T., Togashi, S., Kamioka, H., Amakawa, H., Kagami, H., Hamamoto, T., Yuhara, M., Orihashi, Y., Yoneda, S., Shimizu, H., and others (2000) JNd-1: A neodymium isotopic reference in consistency with LaJolla neodymium. *Chemical Geology*, 168, 279–281.
- Tosdal, R.M., Dilles, J.H., and Cooke, D.R. (2009) From source to sinks in auriferous magmatic-hydrothermal porphyry and epithermal deposits. *Elements*, 5, 289–295.
- Trail, D., Watson, E.B., and Tailby, N.D. (2011) The oxidation state of Hadean magmas and implications for early Earth's atmosphere. *Nature*, 480, 79–82.
- Walker, B.A., Klemetti, E., Gruner, A., Dilles, J., Tepley, F., and Giles, D. (2013) Crystal reaming during the assembly, maturation and waning of an eleven-million-year crustal magma cycle: Thermobarometry of the Aucanquilcha Volcanic cluster. *Contributions to Mineralogy and Petrology*, 165, 663–682.
- Wallace, W.K., Hanks, C.L., and Rogers, J.F. (1989) The southern Kahiltna terrane: Implications for the tectonic evolution of southwestern Alaska. *Geological Society of America Bulletin*, 101, 1389–1407.
- Watson, E.B., and Green, T.H. (1981) Apatite/liquid partition coefficients for the rare earth elements and strontium. *Earth and Planetary Science Letters*, 52, 405–421.
- Watson, E.B., Wark, D.A., and Thomas, J.B. (2006) Crystallization thermometers for zircon and rutile. *Contributions to Mineralogy and Petrology*, 151, 413–433.
- Webster, J.D. (1992) Water solubility and chlorine partitioning in Cl-rich granitic systems: Effects of melt composition at 2 kbar and 800 °C. *Geochimica et Cosmochimica Acta*, 56, 679–687.
- Weis, D., Kieffer, B., Maerschall, C., Barling, J., de Jong, J., Williams, G.A., Hanano, D., Pretorius, W., Mattielli, N., Scoates, J.S., and Goolaerts, A. (2006) High-precision isotopic characterization of USGS reference materials by TIMS and MC-ICP-MS. *Geochemistry, Geophysics, Geosystems*, 7, 30 p.
- Wilke, M., and Behrens, H. (1999) The dependence of the partitioning of iron and europium between plagioclase and hydrous tonalitic melt on oxygen fugacity. *Contributions to Mineralogy and Petrology*, 137, 102–114.
- Wilson, F.H. (1985) The Meshik Arc—An Eocene to earliest Miocene magmatic arc on the Alaska Peninsula. *Alaska Division of Geological and Geophysical Surveys Professional Report*, 88, 14 p. Available: <http://ddgs.alaska.gov/pubs/id/2269/>.
- Wilson, F.H., Hudson, T.L., Grybeck, D., Stoesser, D.B., Preller, C.C., Bickerstaff, D., Labay, K., and Miller, M.L. (2003) Preliminary geologic map of the northeast Dillingham Quadrangle (D-1, D-2, C-1, and C-2), Alaska. U.S. Geological Survey, Open-file Report 03-105, 13 p., scale 1:100,000, <http://pubs.usgs.gov/of/2003/0105/>.
- Wilson, F.H., Hults, C.P., Mull, C.G., and Karl, S.M. (2015) Geologic map of Alaska. USGS Scientific Investigations Map 3340, 1:1,584,000, <https://pubs.er.usgs.gov/publication/sim3340/>.
- Wones, D.R. (1989) Significance of the assemblage titanite + magnetite + quartz in granitic rocks. *American Mineralogist*, 74, 744–749.
- Wooden, J.L., and Barth, A.P. (2010) Coupled elemental and isotopic analyses of polygenetic zircons from granitic rocks by ion microprobe, with implications for melt evolution and the sources of granitic magmas. *Chemical Geology*, 277, 149–159.
- Young, L.E., George, P.S., and Bouley, B.A. (1997) Porphyry copper deposits in relation to the magmatic history and palinspastic restoration of Alaska. *Economic Geology*, Monograph, 9, 306–333.

MANUSCRIPT RECEIVED DECEMBER 8, 2016

MANUSCRIPT ACCEPTED APRIL 28, 2017

MANUSCRIPT HANDLED BY JULIE ROBERGE